

A Journey along the Extruder with Polystyrene

C60 Nanocomposites: Convergence of Feeding Formulations into a Similar Nanomorphology

Gaspar, Hugo; Teixeira, Paulo; Santos, Raquel; Fernandes, Liliana; Hilliou, Loic; Weir, Michael P.; Parnell, Andrew J.; Abrams, Kerry J.; Hill, Christopher J.; Bouwman, Wim

DOI

[10.1021/acs.macromol.6b02283](https://doi.org/10.1021/acs.macromol.6b02283)

Publication date

2017

Document Version

Accepted author manuscript

Published in

Macromolecules

Citation (APA)

Gaspar, H., Teixeira, P., Santos, R., Fernandes, L., Hilliou, L., Weir, M. P., Parnell, A. J., Abrams, K. J., Hill, C. J., Bouwman, W., Parnell, S., King, S. M., Clarke, N., Covas, J. A., & Bernardo, G. (2017). A Journey along the Extruder with Polystyrene: C60 Nanocomposites: Convergence of Feeding Formulations into a Similar Nanomorphology. *Macromolecules*, *50*(8), 3301–3312.
<https://doi.org/10.1021/acs.macromol.6b02283>

Important note

To cite this publication, please use the final published version (if applicable).
Please check the document version above.

Copyright

Other than for strictly personal use, it is not permitted to download, forward or distribute the text or part of it, without the consent of the author(s) and/or copyright holder(s), unless the work is under an open content license such as Creative Commons.

Takedown policy

Please contact us and provide details if you believe this document breaches copyrights.
We will remove access to the work immediately and investigate your claim.

1
2
3 **A Journey Along the Extruder with Polystyrene:C₆₀**
4
5
6 **Nanocomposites: Convergence of Feeding Formulations into a**
7
8
9 **Similar Nano-Morphology**
10

11 Hugo Gaspar¹, Paulo Teixeira¹, Raquel Santos¹, Liliana Fernandes¹, Loic Hilliou¹, Michael P.
12 Weir², Andrew J. Parnell², Kerry J. Abrams³, Christopher J. Hill⁴, Wim G. Bouwman⁵,
13 Steven R. Parnell⁵, Stephen M. King⁶, Nigel Clarke², José A. Covas^{1,*}, Gabriel Bernardo^{1,*^ψ}
14
15
16
17
18
19
20
21

22 ¹Institute for Polymers and Composites/I3N, University of Minho, 4800-058 Guimarães,
23 Portugal
24

25 ²Department of Physics and Astronomy, The University of Sheffield, Sheffield S3 7RH,
26 United Kingdom
27
28
29

30 ³Department of Materials Science and Engineering, The University of Sheffield, Sheffield S1
31 3JD, United Kingdom
32
33

34 ⁴Department of Biomedical Science, The University of Sheffield, Sheffield S3 7HF, United
35 Kingdom
36
37

38 ⁵Faculty of Applied Sciences, Delft University of Technology, Mekelweg 15, 2629 JB Delft,
39 Netherlands
40
41

42 ⁶ISIS Pulsed Neutron Source, STFC Rutherford Appleton Laboratory, Harwell Campus,
43 Didcot, OX11 0QX, United Kingdom
44

45 *Corresponding authors: gabriel.bernardo@dep.uminho.pt; jcovas@dep.uminho.pt
46
47

48 ^ψPresent address: Department of Physics and Astronomy, The University of Sheffield,
49 Sheffield S3 7RH, United Kingdom
50
51
52
53
54
55
56
57
58
59
60

Abstract

In this work we investigated the effect of the feeding formulation (pre-mixed powders of pure components versus solvent-blended mixture) of polystyrene-C₆₀ composites on the dispersion and re-agglomeration phenomena developing along the barrel of a twin screw extruder. The dispersion of C₆₀ in the PS matrix is studied over different length-scales using a combination of optical microscopy, Spin-Echo-Small Angle Neutron Scattering (SESANS), Small Angle Neutron Scattering (SANS), Small Angle X-ray Scattering (SAXS) and Wide Angle X-ray Scattering (WAXS). When a solvent-blended mixture is used as the feeding formulation, the inlet material contains essentially molecularly dispersed C₆₀ as revealed by the nano-domains with very small phase contrast. However, C₆₀ re-agglomeration occurs along the extruder, creating a morphology still containing only nano-domains but with much higher phase contrast. In the case of mixed powders, the material evolves from the initial macroscopic mixture of pure polystyrene and C₆₀ into a composite simultaneously containing micro- and nano-aggregates of C₆₀ as well as C₆₀ molecularly dispersed in the matrix. Our results show that the two different initial feeding formulations with widely different initial morphologies converge along the extruder, through opposite morphological pathways, into a similar final nanomorphology which is dictated by the interplay between the thermodynamics of the system and the flow. Correlations between the morphological evolution along the extruder and the thermo-rheological properties of the composites are identified.

Keywords: Nanocomposites; Small Angle Neutron Scattering (SANS); Spin-Echo-SANS (SESANS); Small Angle X-ray Scattering (SAXS); fullerene C₆₀; extrusion

1. Introduction

Polymer nanocomposites containing carbon nanoparticles such as graphenes^{1, 2}, carbon nanotubes³⁻⁷ and fullerenes⁸ open a new horizon for polymeric-based materials. These materials benefit from a synergistic combination of useful polymer properties, such as low density, flexibility, ease of processing and cost efficiency, with nanoparticles that not only significantly enhance the mechanical, electrical, and thermal properties of the resulting composite⁹, as well as create novel functionalities. Although the homogeneous dispersion and distribution of carbon nanoparticles in a polymer matrix is generally desired to maximize performance, some level of particle aggregation can be advantageous in specific applications^{10, 11}. Though property improvements have been achieved in a variety of nanocomposites, carbon nanoparticle dispersion remains difficult to control, with both thermodynamic and kinetic processes playing significant roles.

The dispersion of carbon nanotubes and graphenes is complicated by their strong van der Waals interactions, chemical inertia that creates weak interfaces with most polymers, as well as difficulty to control initial size and shape of these nanoparticles. These parameters influence the cohesiveness of the agglomerates and have been related to dispersion routes such as rupture and erosion^{12, 13}. Conversely, fullerene C₆₀ (also known as buckminsterfullerene) has a very well defined size and shape: it is a bucky-ball with a diameter of 0.7 nm^{14, 15}. When replacing graphenes or carbon nanotubes by fullerenes in a polymer composite, particle size and geometry change (these being associated with entropic changes) while the differences in enthalpic interactions between the particles and the matrix are kept at a minimum. For this reason, polymer composites with C₆₀ can be used as model systems to help understand the dispersion of carbon nanoparticles.

1
2
3 In the last two decades, polystyrene (PS) composites containing fullerene nanoparticles
4
5 have been the subject of a number of studies¹⁵⁻³³ reporting improvements in properties such
6
7 as electrical conductivity^{22, 23}, thermal stability²⁴⁻²⁷ and permeability^{28, 29}. The impact of C₆₀
8
9 loading and sample preparation conditions on the corresponding glass transition temperature
10
11 (T_g) and melt viscosity, has also received attention^{16, 19, 34}.

14 Campbell et al²¹ used wide-angle X-ray scattering (WAXS) to determine the miscibility
15
16 limit of C₆₀ in PS as being ~1 wt%. In this context miscibility is understood as an absolute
17
18 thermodynamic value associated with molecular homogeneity and which is reversible and
19
20 independent of the pathway followed from aggregates to molecular dispersion, i.e. it is a
21
22 maximum value that is independent of processing. An identical miscibility threshold was
23
24 determined by Sanz et al³⁴, using a combination of microscopy, SANS and WAXS
25
26 experiments. Additionally, these authors also determined a dispersibility threshold of ~4 wt%
27
28 C₆₀, where this is the maximum C₆₀ loading associated with the maximum observed increase
29
30 in the T_g of the composites. Loadings beyond this concentration gradually reverted the
31
32 composite T_g towards the neat PS value. Increases in T_g with C₆₀ loadings in PS composites
33
34 were also reported by Weng et al³² and by Wong et al¹⁹, with the latter also concluding that
35
36 beyond 1 wt% nanoparticle concentration, the C₆₀ is aggregated in polydispersed aggregates.
37
38 Self-assembly of C₆₀ into clusters within PS-C₆₀ thin films was also reported, with the size of
39
40 the clusters becoming macroscopic for C₆₀ concentrations in the range 3 wt% – 4 wt% C₆₀³⁰.

46 The impact of C₆₀ on the melt viscosity of PS-C₆₀ composites was studied by Tuteja et al
47
48¹⁶. They showed that a viscosity reduction in the PS-C₆₀ nanocomposites may occur if the
49
50 polymer is entangled ($M > M_c$, where M_c is the critical molecular mass critical mass for
51
52 entanglement coupling) and if the average interparticle half-gap (h) is less than the polymer
53
54 size (i.e. $h < R_g$), where $h/a = [\Phi_m/\Phi]^{1/3} - 1$, Φ_m being the maximum random packing volume
55
56 fraction (~0.638) and a being the particle radius (~0.4 nm). For non-entangled polymer melts
57
58
59
60

1
2
3 ($M < M_c$), a viscosity increase is observed upon the addition of C₆₀. In practice, the authors
4
5 observed a viscosity decrease in well dispersed fullerene-polystyrene nanocomposites
6
7 prepared via rapid precipitation from solution and using a PS with Mw= 393 kDa. On the
8
9 other hand, a viscosity increase was observed when using a PS with Mw=19.3 kDa.
10

11
12 In most of the preceding studies, PS-C₆₀ blending was achieved through the use of
13
14 solvents, using methods such as solvent casting or rapid precipitation from solution. Despite
15
16 the fact that in the commodity plastics industry melt extrusion is a ubiquitous process for the
17
18 manufacturing of polymer nanocomposites, with solvents rarely being used, in the scarce
19
20 literature studies in which polymer-C₆₀ blending was performed in an extruder no attempts
21
22 were made to assess the dispersion achieved²⁷. Therefore, there is an obvious fundamental
23
24 and practical interest in studying how C₆₀ nanoparticles can be mixed with polystyrene in a
25
26 melt extruder.
27
28

29
30 In this work, we conduct a detailed investigation of the dispersion of fullerene C₆₀ in
31
32 polystyrene composites along an intermeshing co-rotating twin-screw extruder. We study and
33
34 compare two different types of melt-processed PS-C₆₀ composites that were prepared using
35
36 identical C₆₀ loadings (1 wt%) and processing conditions (flow rate = 130 g.h⁻¹, screw speed
37
38 = 80 rpm; extruder and die set temperature = 200 °C), but which differ widely on the quality
39
40 of dispersion of the initial material: (i) mixed powders of pure polystyrene and pure C₆₀ and
41
42 (ii) a solvent pre-processed PS-C₆₀ blend. The morphological characterization of the
43
44 composites was performed using both direct and indirect characterization techniques. Five
45
46 direct morphological characterization techniques were used to probe four different length-
47
48 scale regimes, namely: optical microscopy for the ~ 1 mm – 1 μm range; spin-echo small
49
50 angle neutron scattering (SESANS)³⁵ for the ~ 20 μm – 200 nm range; small angle neutron
51
52 scattering (SANS) and small angle x-ray scattering (SAXS) for the ~ 200 nm – 1 nm range
53
54 and wide angle x-ray scattering (WAXS) for the sub-nanometer range. Additionally, the
55
56
57
58
59
60

1
2
3 composites were characterized by differential scanning calorimetry (DSC) and rheological
4
5 measurements, as indirect morphological characterization techniques, to provide an overall
6
7 understanding of the processing-structure-property relationships in these model polymer-
8
9 fullerene systems.
10

11
12 This paper is organized as follows. We first describe the sample preparation methods.
13
14 Then we characterize the dispersion of C₆₀ in the composite samples using optical
15
16 microscopy, SESANS, SANS, SAXS and WAXS. Next, we study the variation of the glass
17
18 transition temperature with sample preparation conditions and we characterize the samples
19
20 rheologically. Finally, we discuss and rationalize all the results obtained.
21
22

23 24 25 **2. Experimental Section** 26

27 28 *2.1 Materials* 29

30
31 The C₆₀ fullerene used in this work was supplied by Solenne BV (> 99.5% purity, Mw =
32
33 720.64 g.mol⁻¹ and density = 1.65 g.cm⁻³). The polystyrene was purchased from Sigma
34
35 Aldrich (catalog # 430102) with average Mw~192.000, MFI = 6.0-9.0 g/10 min (200°C/5kg)
36
37 and density of 1.05 g.cm⁻³ at 25 °C. The polymer R_g is approximately 12 times larger
38
39 (estimated from $R_g \cong 0.27M_w^{1/2}$ ³⁶) than the diameter of C₆₀ (~1 nm).
40
41
42

43 44 *2.2 Nanocomposite preparation* 45

46
47 Two different types of PS-C₆₀ formulations were prepared as feeding material for the twin
48
49 screw extruder: (a) 1.0 wt% C₆₀ was simply mechanically mixed with PS (hereafter simply
50
51 referred to as “mixed powders”) and (b) mixtures with 1.0 wt% C₆₀ were prepared by solution
52
53 blending followed by co-precipitation in a non-solvent (hereafter referred to as “pre-solvent
54
55 blended”).
56
57
58
59
60

1
2
3 In the preparation of the mixed powders formulation, the granulated polystyrene was
4 milled into a fine powder and then thoroughly mixed with the, as purchased, fine C₆₀ powder
5 in a rotating mixer.
6
7
8

9
10 In the preparation of the pre-solvent blended formulation, appropriate amounts of PS and
11 C₆₀ were dissolved in toluene, while stirring at 80 °C for 4 hours. Then, the solution was
12 added dropwise into a 5-fold volume excess of pre-cooled methanol (T < 0°C) under
13 continuous stirring, to enable the co-precipitation of the PS-C₆₀ composite. The solids were
14 vacuum filtered from methanol using a nylon membrane filter with a pore size of 0.45 μm
15 (Whatman, cat no. 7404-004) and washed with cold methanol. This was followed by drying
16 at ~100 °C and 10⁻² mbar for several hours, until no mass changes were detected using a
17 balance with a precision of ±0.01g. Upon drying, light purple fiber composites were obtained.
18 The yield of composite preparation was ~ 100%, showing that no C₆₀ and polystyrene losses
19 had occurred. The total amount of pre-solvent blended formulation prepared was ~35 g (after
20 drying). Finally, the fibrous composite was milled into a fine light purple powder.
21
22
23
24
25
26
27
28
29
30
31
32
33
34

35 The two types of feeding formulations were then melt processed in a prototype co-rotating
36 intermeshing twin-screw extruder of modular construction (Figure S.I.1.(a) in Supporting
37 Information), designed to process small amounts of material (in the range of 30-300 g/h)
38 while retaining the same characteristics of larger equipment. The screws have a diameter of
39 13 mm and an L/D ratio of 27 (Figure S.I.1.(b) in Supporting Information). The screw profile
40 is built by sliding along a shaft conveying (with distinct pitches and lengths) and kneading
41 elements (that can be stacked with variable staggering angles to induce different
42 hydrodynamic stress levels and, therefore, variable balances of distributive/dispersive
43 mixing). The barrel contains nine material sampling ports, evenly distributed along its length.
44 These are manually operated rotary valves which allow one to quickly remove small volumes
45 of material from within the extruder during steady state operation^{37, 38}. A miniaturized
46
47
48
49
50
51
52
53
54
55
56
57
58
59
60

1
2
3 prototype volumetric feeder is positioned upstream. The screw profile used in this work
4
5 contained two kneading zones consisting of four 3 mm thick kneading disks staggered at -30°
6
7 (for intensive mixing) separated by a conveying zone. The flow channels had a maximum
8
9 depth of 1.5 mm so that shear rates were relatively high, even at low screw speeds.
10

11
12 Each PS-C₆₀ mixture was compounded at a flow rate of 130 g/h, with the screws rotating
13
14 at 80 rpm. The temperature profile along the barrel and the slit die (5 mm x 1 mm) was kept
15
16 at a constant 200 °C for all the processing experiments. In order to track the quality of the
17
18 mixing along the extruder, spherically-shaped composite samples in their molten state were
19
20 collected at sampling ports P2 and P9 during steady state extruder operation. These molten
21
22 samples were then sandwiched between two Teflon sheets placed between two metal plates
23
24 and slightly compressed, while cooling down to room temperature, into approximately
25
26 circular disks with thickness ~1.5 mm and diameter ~ 20 mm (see Figure S.I.2 in Supporting
27
28 Information). These samples, hereafter simply referred to as samples P2 and P9 depending on
29
30 the sampling port from which they were collected, as well as the extruded ribbons collected
31
32 after air cooling and winding were then stored for subsequent characterization. To keep the
33
34 extrusion line running continuously, the lowest possible draw-down (i.e., the ratio between
35
36 the linear velocity of the winder and the extrudate velocity) was applied.
37
38
39

40
41 Additionally, reference samples with C₆₀:PS weight ratios 1:99 were prepared by
42
43 compression molding: (i) a mixture of the pure powders at 170 °C and 10 MPa during 5
44
45 minutes (1 sample produced); (ii) powders of the solvent blended composite at 90 °C and 170
46
47 °C and 10 MPa during 5 minutes (2 samples produced). These three reference samples were
48
49 also stored for subsequent characterization.
50
51

52
53 All the samples are shown in Figure S.I.2 in Supporting Information. The initial sample
54
55 compression molded from mixed powders is mostly colourless and transparent, albeit
56
57 containing a few macroscopic black spots in it. The initial pre-solvent blended sample is
58
59
60

1
2
3 purple and transparent. The samples from mixed powders collected at P2, P9 and ribbon are
4
5 all dark brown and optically opaque. The samples from pre-solvent blend collected at P2, P9
6
7 and ribbon are light brownish and still optically transparent to some degree.
8
9

10 2.3 *Nanocomposites characterization*

11 2.3.1. *Optical microscopy*

12
13
14 The agglomerate size distribution in the initial, i.e. before melt compounding, pre-solvent
15
16 blended and mixed powder formulations was determined by light transmission optical
17
18 microscopy (O.M.) using a BH2 Olympus microscope coupled to a Leica DFC 280 camera,
19
20 with a 1.6 x ocular and 20 x objective magnification. For microscopy observations, the
21
22 feeding formulations (in powder form) were softened at 160 °C and spread onto a glass slide.
23
24
25
26
27

28 The evolution of dispersion along the extruder was estimated by O.M. For this, 10 μm thin
29
30 sections were cut from samples at room temperature with a Leitz 1401 microtome using glass
31
32 knives with an angle of 45°. The extruded tapes were molded in an epoxy resin and cut
33
34 perpendicular to the flow direction. Micrographs were acquired using the same microscopy
35
36 equipment and under similar magnifications. To obtain sufficient statistics, at least six
37
38 micrographs were analyzed using ImageJ[®] Software, leading to an investigated total area of
39
40 2.1 mm².
41
42
43

44 The level of dispersion was quantified in terms of Area ratio (Ar), which balances the total
45
46 area of agglomerates and the total area analyzed, and cumulative relative distribution of the
47
48 agglomerates (C_{C60}). This is determined by summing the areas of the individual agglomerates
49
50 in ascending area order and dividing by the total area of agglomerates. In particular, the size
51
52 of the larger agglomerate contained in 75% (A_{χ75}) and 90% (A_{χ90}) of the total area of
53
54 agglomerates were followed.
55
56
57
58
59
60

2.3.2. Spin-Echo Small Angle Neutron Scattering (SESANS)

Spin-Echo Small Angle Neutron Scattering (SESANS) is a relatively new technique to measure structures of materials. Structures can be determined over three orders of magnitude in length scale, from 10 nm to 20 μm . This is two orders of magnitude larger than conventional SANS and comparable to what may be studied with light scattering or OM, though with the complementary benefits afforded by the use of neutrons such as contrast and probing the bulk. However, like O.M., and unlike SANS (or SAXS), SESANS measures in real space.

Briefly, SESANS uses a series of magnetised permalloy films and magnetic fields to encode the scattering angle information in the spin precession of a beam of polarized neutrons. Neutrons scattered through different angles traverse magnetic fields of different lengths and thus precess differently to the unscattered neutrons. The structural length scale probed depends upon the applied magnetic field strength, hence varying the magnetic field strength provides tunability over a range of length scales, termed the spin-echo length.

The SESANS measurements reported here were performed at the Reactor Institute Delft (TU Delft, Netherlands), using a beam monochromatised (using a pyrolytic graphite crystal) to a wavelength $\lambda=2.06 \text{ \AA}$ ³⁵. The pre-solvent blend sample was measured for 4 hours whilst the sample from mixed powders was measured for ~12 hours over the same spin-echo length range.

2.3.3. Small Angle Neutron Scattering (SANS)

Small-angle neutron scattering (SANS) measurements were performed at the LOQ diffractometer at the ISIS Pulsed Neutron Source (Rutherford Appleton Laboratory, Oxfordshire, UK) with a polychromatic incident beam of $\lambda = 2 - 10 \text{ \AA}$ and fixed sample-to-detector distance of 4 m, to provide a scattering vector range of $0.009 < q < 0.25 \text{ \AA}^{-1}$, where

1
2
3 $q=(4\pi/\lambda)\sin(\theta/2)$ and θ is the scattering angle. Due to the high carbon to hydrogen content in
4
5 C_{60} , there is a naturally high neutron scattering length density contrast with the hydrogenous
6
7 polystyrene polymer removing the need for isotopic substitution (deuteration). However,
8
9 there is a greater degree of incoherent background scattering from the matrix that degrades
10
11 the signal-to-noise, particularly at larger q values.
12
13

14
15 The samples P2 and P9 were ~ 1.5 mm thick and the extruded ribbons were ~ 0.7 mm
16
17 thick although their exact thicknesses were measured by a micrometer and those values used
18
19 in the data reduction procedure to ensure proper intensity scaling. Samples were mounted on
20
21 a computer-controlled sample changer and SANS patterns were recorded at room temperature
22
23 for approximately 90 min/sample. Each raw scattering data set was then radially-averaged,
24
25 corrected for the detector efficiency, sample transmission and background scattering and then
26
27 converted to scattering cross-section data and plotted on an absolute scale ($\partial\Sigma/\partial\Omega$ vs q) using
28
29 Mantid software³⁹. For convenience, we shall follow the normal convention of referring to
30
31 $\partial\Sigma/\partial\Omega$ as intensity (I). The corrected data were then fitted to appropriate models using
32
33 SasView software (Version 3.1.1)⁴⁰. The neutron scattering length densities of hydrogenous
34
35 PS and of C_{60} are respectively, $\rho_N(H-PS) = 1.41 \times 10^{-6} \text{ \AA}^{-2}$ and $\rho_N(C_{60}) = 5.60 \times 10^{-6} \text{ \AA}^{-2}$ and
36
37 therefore $\Delta\rho_N=4.09 \times 10^{-6} \text{ \AA}^{-2}$.
38
39
40
41

42 2.3.4. Small Angle X-Ray Scattering (SAXS)

43
44
45 SAXS measurements were performed in-house on a Bruker instrument (NanoStar,
46
47 Department of Chemistry, University of Sheffield, UK) equipped with a microfocus Cu-K α
48
49 source (8 keV, $\lambda = 1.54 \text{ \AA}$; Xenocs, France), collimating system with motorized scatterless
50
51 slits (Xenocs, France) and a HiStar 2D multiwire gas detector (Siemens/Bruker). Scattering
52
53 patterns were corrected for the detector's dark current, spatial distortion, flat field and
54
55 normalized using sample thickness, exposure time, sample transmission and the detector
56
57
58
59
60

1
2
3 normalization coefficient. The electron densities of hydrogenous PS and of C₆₀ are
4
5 respectively, $\rho_X(H-PS) = 9.56 \times 10^{-6} \text{ \AA}^{-2}$ and $\rho_X(C_{60}) = 1.40 \times 10^{-5} \text{ \AA}^{-2}$ and therefore $\Delta\rho_X =$
6
7 $4.44 \times 10^{-6} \text{ \AA}^{-2}$.
8
9

10 11 *2.3.5. Wide Angle X-Ray Scattering*

12
13 WAXS measurements, of samples P9 from both mixed powders and solvent processed
14
15 blend, were performed on a Xeuss 2.0 SAXS/WAXS laboratory beamline using a liquid
16
17 Gallium MetalJet (Excillum) x-ray source (9.2 keV, $\lambda = 1.34 \text{ \AA}$). The scattered X-rays were
18
19 detected using a Pilatus3R 1M detector. Scattering from the samples was collected at room
20
21 temperature for 3 minutes.
22
23

24 25 *2.3.6. Differential Scanning Calorimetry*

26
27
28 Differential Scanning Calorimetry (DSC) experiments were performed on a Perkin Elmer
29
30 Pyris-1 calorimeter under nitrogen where temperature and heat capacity were calibrated using
31
32 a sapphire standard. Thermal history was eliminated by ramping from 25 to 150 °C at 10
33
34 °C.min⁻¹, isothermal annealing at 150 °C for 2 minutes, then cooling to 30 °C at 10°C.min⁻¹.
35
36 Two heating-cooling cycles were run. The glass transition temperature T_g was computed from
37
38 the second heating run following the half-Cp extrapolation method. Error bars in T_g are
39
40 estimated by the maximum deviation of three independent measurements.
41
42
43

44 45 *2.3.7. Rheometry*

46
47 Disks were loaded between the parallel plates (diameter 25 mm) of a stress-controlled
48
49 rotational rheometer (ARG2, TA Instruments) at a temperature of 200 °C under air. Time was
50
51 left for the samples to thermally stabilize and adjust to the defined gap between the parallel
52
53 plates, as inferred from the on-line reading of the normal force relaxation. A time sweep was
54
55 first performed at 1 Hz with a deformation of 0.1% (corresponding to the linear regime of
56
57
58
59
60

viscoelasticity as inferred from separate strain sweep experiments performed at 1 Hz) to confirm the thermal stability of all samples within 20 minutes. Then a new sample was loaded and equilibrated as mentioned above, for the recording of a mechanical spectrum using a frequency sweep performed with a deformation of 0.1%.

3. Results and Discussion

As an aid to the analysis and discussion of our experimental results, we start by showing in Figure 1 an idealized schematic of the different possible stages of C_{60} dispersion in a polymer matrix.

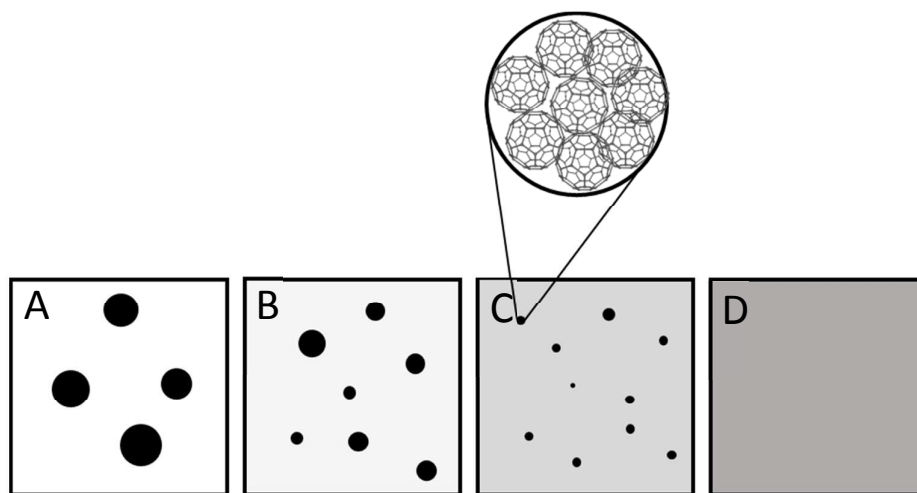


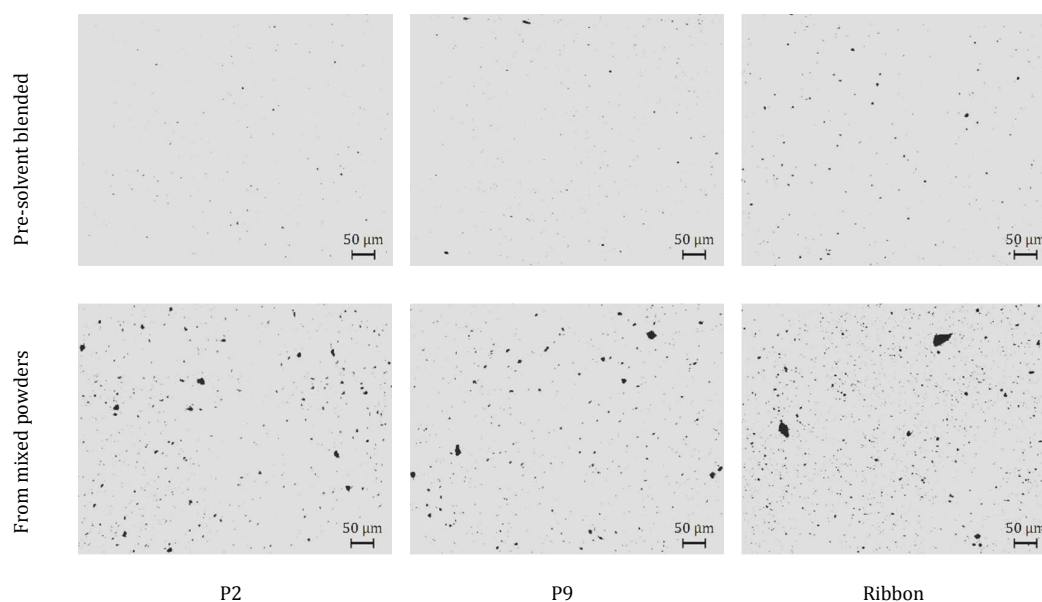
Figure 1. Idealized schematic of C_{60} dispersion in the polymer matrix along the extruder, starting from macroscopic agglomerates of C_{60} in a matrix of pure polymer and ending with an idealized mixture of individual C_{60} molecules homogeneously dispersed in the polymer matrix.

There are two extreme situations, namely situation A in which macroscopic and microscopic agglomerates of C_{60} coexist in a matrix of pure polymer and situation D consisting of an idealized mixture of individual C_{60} molecules homogeneously dispersed in

1
2
3 the polymer matrix. Two intermediate cases (B and C) correspond to a mixture of
4 microscopic and nanoscopic agglomerates of C_{60} in a polymer matrix containing some
5 microscopic and nanoscopic agglomerates of C_{60} in a polymer matrix containing some
6 molecularly dispersed C_{60} and to a mixture of nanoscopic agglomerates in a polymer matrix
7 containing a considerable amount of molecularly dispersed C_{60} , respectively.
8
9

10
11
12 The level of dispersion of C_{60} in the initial feeding formulations and in the samples
13 collected along the extruder was first investigated by optical microscopy (O.M.), as shown in
14 Figure 2 and in Figure S.I.3. in Supporting Information.
15
16
17
18
19

20 **(a)**



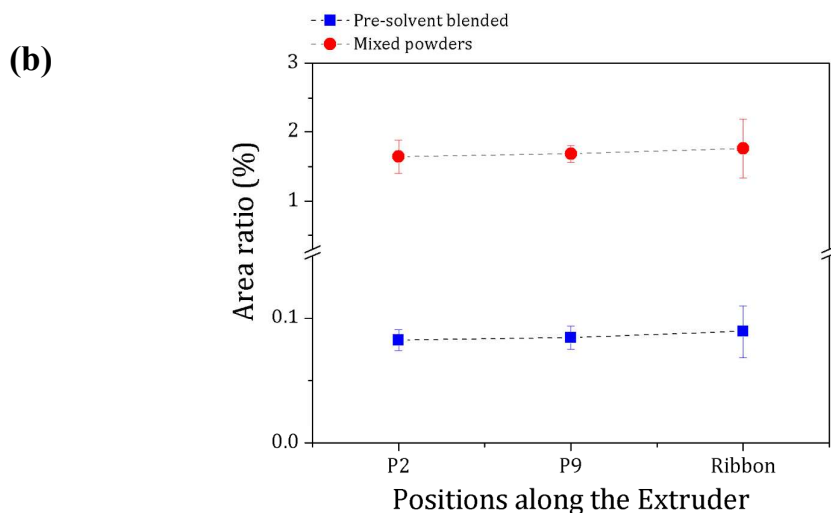


Figure 2. (a) Morphology development of PS nanocomposites containing 1 wt. % of C_{60} along the twin-screw extruder; (b) Area ratio evolution along the twin-screw extruder of PS nanocomposites containing 1 wt. % of C_{60} .

Figure S.I.3. shows optical microscopy images of the initial feeding formulations. The image of the “mixed powders” feeding formulation shows large black aggregates in a matrix of essentially pure polystyrene. Overall this formulation shows both a poor dispersion and poor distribution of the aggregates. By contrast, on the image of the “solvent-blended” feeding formulation, although some randomly distributed darker spots are visible, these are not large black aggregates. These darker spots most likely result from some possible heterogeneities (regions with different PS: C_{60} ratio) inherent to the precipitation process used in the preparation of this composite. Also visible in the “solvent-blended” figure is a larger, approximately circular, feature with $\sim 50 \mu\text{m}$ diameter which corresponds to material that did not melt during the preparation of the optical microscopy samples.

The morphology development of PS nanocomposites containing 1 wt. % of C_{60} along the extruder is presented in Figure 2(a). As clearly shown, the extruded samples prepared from mixed powders contain a large number of microscopic aggregates. By contrast, in the extruded samples prepared from pre-solvent blend the number and size of microscopic

features is much smaller. Figure 2(b) displays the corresponding evolution of the area ratio and the dispersion characterization results are summarized in Table 1. As shown in Figure 2 and Table 1, in extruded samples from both mixed powders and pre-solvent blend, the area ratio remains approximately constant along the extruder.

It is well accepted that dispersion of solid agglomerates in a molten matrix occurs when the hydrodynamic stresses developed during flow are larger than the cohesive strength of the agglomerates. This balance is usually quantified by the fragmentation number, F_a . It has been suggested that when F_a is large, dispersion is dominated by the rupture of the agglomerates into successively smaller aggregates. When F_a is small, erosion should prevail. This is a much slower dispersion route, whereby small aggregates or individual particles detach from the agglomerates. Both phenomena were reported in studies of the dispersion of carbon nanotubes and graphite nanoplates^{41, 42}. In the present work, as the area ratio remained constant along the extruder, this means that no substantial rupture took place, but some dispersion may have developed via erosion, as in this case the large agglomerates are still visible by optical microscopy.

Position	Pre-solvent blended			From mixed powders		
	$A_{\chi 75\%}$ (μm^2)	$A_{\chi 90\%}$ (μm^2)	N (per mm^2)	$A_{\chi 75\%}$ (μm^2)	$A_{\chi 90\%}$ (μm^2)	N (per mm^2)
P2	16.91	24.07	88 ± 10	59.31	161.88	988 ± 137
P9	17.48	28.95	88 ± 16	71.34	178.22	980 ± 76
Ribbon	18.86	33.84	92 ± 16	87.43	374.48	1020 ± 235

Table 1. Optical microscopy dispersion characterization results for PS nanocomposites containing 1.0 wt. % of C_{60}

The SESANS data from two nanocomposites extracted from port P9 is shown in Figure 3. The data from the mixed powder sample has been fitted to a model of monodispersed

particles using the Gaussian approximation formalism detailed by Andersson et al.⁴³ and the resulting fit is also shown in Figure 3.

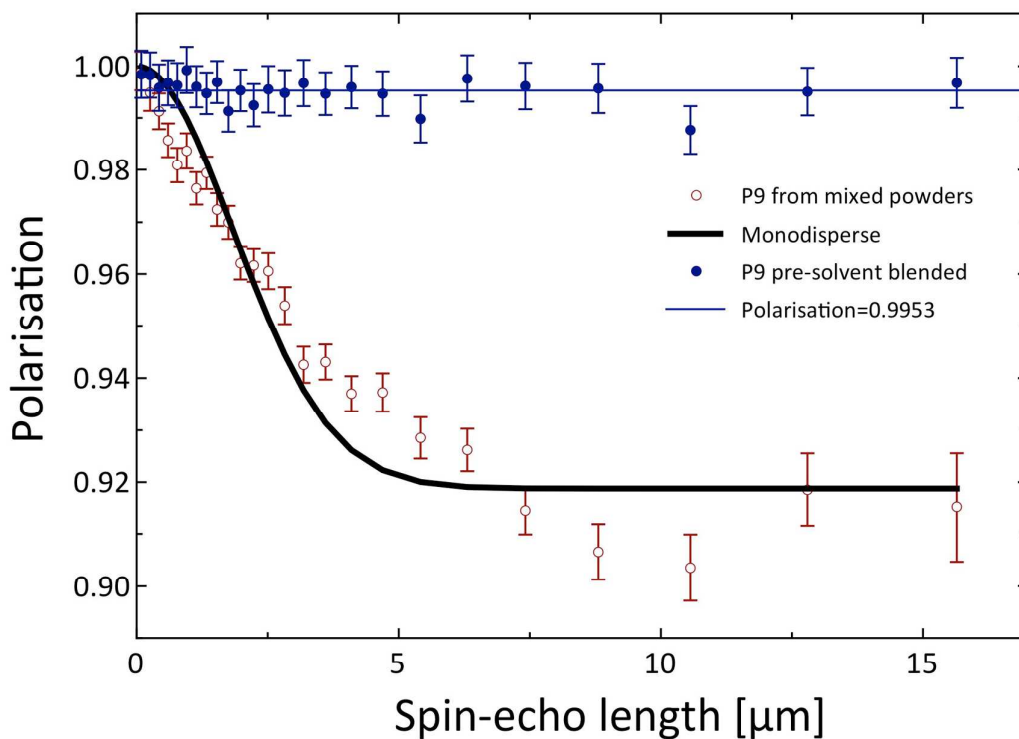


Figure 3. Spin-Echo-SANS signals, expressed as the depolarisation ratio P/P_0 , of extruded PS-C₆₀ nanocomposites extracted from sampling port #9. The black line is a fit to a monodisperse sphere model whilst the blue line is a constant illustrating a small depolarisation over those length scales probed in the pre-solvent blended sample.

This modelling approach is used as the system is low concentration and no consideration of a structure factor is necessary. The best fit to the data, in which the radius was the only free parameter, was found for particles of radius $2.83 \pm 0.10 \mu\text{m}$. The scattering length densities were fixed at the values quoted in Table 2, as derived from the SANS data analysis detailed below. We note in passing that the extended tail of the data at longer spin echo lengths suggests that there is in fact a dispersion in the particle sizes of the agglomerates.

No structure was observed in the pre-solvent blended sample on SESANS length scales, however some depolarisation is observed $\langle P \rangle = 0.9953$ which can be attributed to very small

1
2
3 structures (well below the micron level observed in the mixed powder sample). In the
4
5 micrographs obtained by optical microscopy there is some evidence for larger structures in
6
7 the pre-solvent blended sample. However, Figure 2(b) shows that the area ratio is one order
8
9 of magnitude smaller than that of the mixed powders. The change in SESANS polarization
10
11 ratio as a function of spin echo length is given by $P = P_0 \exp(-\Sigma_t [G(z)-1])$, where $G(z)$ is the
12
13 projection of the density distribution along the measurement axis and the term Σ_t (the fraction
14
15 of neutrons that are scattered only once) in a binary mixture scales with the volume fraction
16
17 Φ as $\Phi(1-\Phi)$. Hence if one assumes that the area ratio of agglomerates measured at the
18
19 surface is consistent with their volume fraction in the bulk then the change in polarisation
20
21 ratio would be of the order 1%, which is at the limits of detection for the instrument used.
22
23

24
25
26 In order to probe the bulk nano-morphology of the composite samples at length-scales
27
28 from $\sim 1 - 200$ nm, we used SANS and the results are shown in Figure 4. In SANS, the
29
30 intensity is proportional to the number, size and contrast of the scattering entities in a sample,
31
32 while the q -dependence of the intensity is related to their shape and local arrangement. So in
33
34 our composites it is the scattering from the C_{60} that dominates the SANS, not the
35
36 hydrogenous PS (which would be expected to contribute a mostly flat background).
37
38

39
40 We have started our analysis of the SANS data by determining if processing induces any
41
42 nanoscale orientation in our samples. In the Supporting Information, Figure S.I.4.(a) shows
43
44 the 2D SANS patterns from extruded ribbons processed from both a pre-solvent blend and
45
46 from mixed powders, and in Figure S.I.4.(b) we show the corresponding intensity ratios
47
48 $I(Q_V)/I(Q_H)$ as a function of q for the vertical and horizontal quadrants of the 2D patterns. As
49
50 clearly shown, the nanoscale distribution of C_{60} aggregates in the extruded ribbons is
51
52 isotropic. Accordingly, the SANS data were circularly-averaged to produce 1D graphs of
53
54 intensity vs q .
55
56

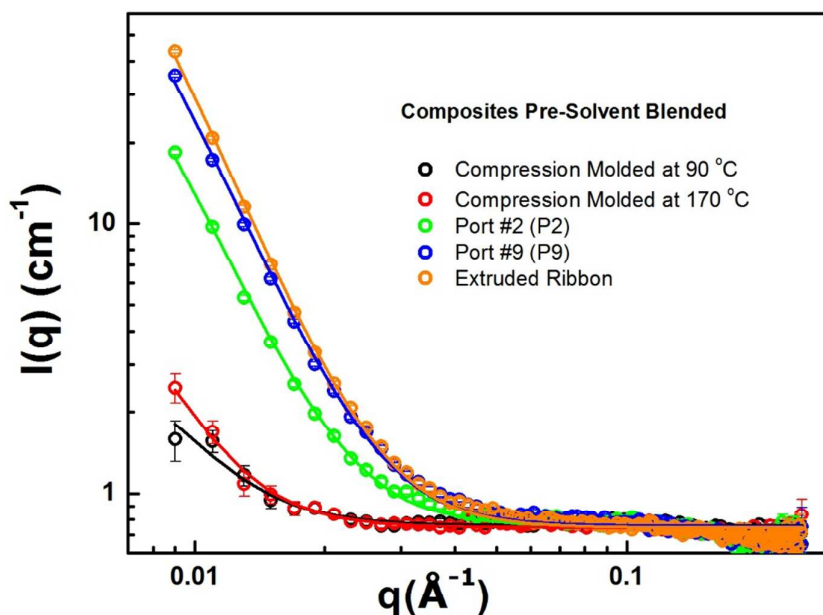
57
58 As shown in Figure 4(a) for the pre-solvent blended composite, five different samples
59
60

1
2
3 were analyzed using SANS, namely: (a) a compression molded sample annealed at 90 °C for
4
5 5 minutes; (b) a similarly compression molded sample annealed at 170 °C for 5 minutes; (c)
6
7 an extruded sample collected at P2; (d) an extruded sample collected at P9 and (e) an
8
9 extruded ribbon.
10

11
12 As can be seen in Figure 4(a), the neutron scattering intensity $I(q)$ of the compression
13
14 molded sample annealed at 90 °C for 5 minutes is very weak and only increases slightly when
15
16 the annealing temperature increases to 170 °C. Our goal on testing these samples at these two
17
18 temperatures (90 °C and 170 °C), intermediate between room temperature and the extrusion
19
20 temperature (200 °C), was to study the effect of temperature alone on the nano-morphology
21
22 of the composite samples as they are heated at the very beginning of the extruder.
23
24
25
26
27
28
29
30

31
32
33
34
35
36
37
38
39
40
41
42
43
44
45
46
47
48
49
50
51
52
53
54
55
56
57
58
59
60

(a)



(b)

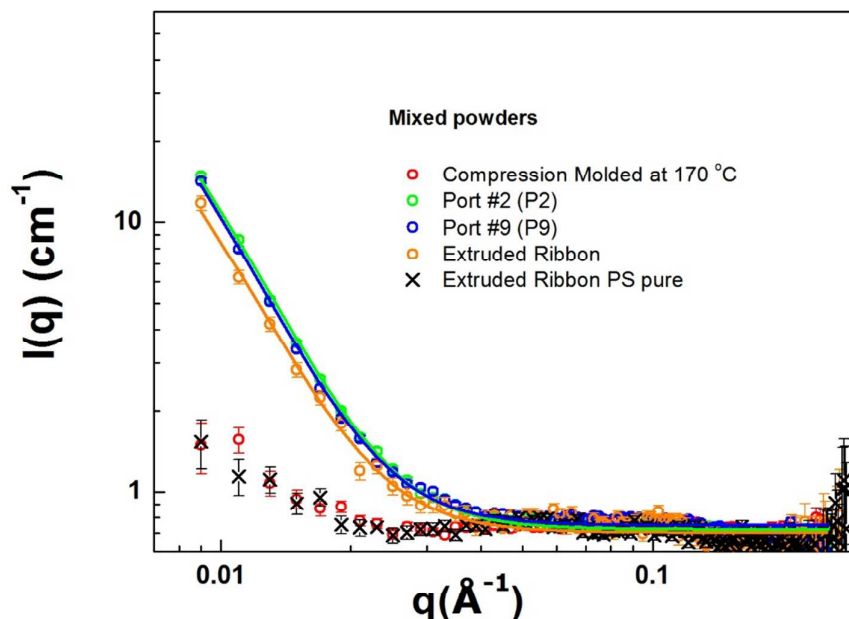


Figure 4. SANS data from extruded PS-C₆₀ nanocomposites (identical scales have been used for ease of comparison): (a) Pre-solvent blended; (b) Prepared from mixed powders of PS and C₆₀.

When the composites are fed into the extruder an abrupt increase of nearly 1 order of magnitude in scattering intensity occurs in the early stages of the extrusion process, as revealed by a comparison between the two previous samples and the sample P2. Indeed, it can be seen that the scattering intensity continues to increase further along the extruder, reaching a maximum value in the extruded ribbon.

Figure 4(b) presents the SANS data for the corresponding composites prepared from mixed powders of the pure components PS and C₆₀. Also shown for comparison are the background (incoherent) SANS scattering of a ribbon of pure PS extruded under the same conditions, as well as the SANS of a sample prepared by compression molding at 170 °C consisting of C₆₀ and PS powders in the weight ratio 1:99. This sample corresponds to the unmixed reference, i.e. a sample in which C₆₀ and PS are not intermixed (situation A in

1
2
3 Figure 1). As seen in Figure 4(b), there is again an almost 1 order of magnitude increase in
4
5 scattering intensity in the early part of the extruder, i.e. from the powder mixture at the inlet
6
7 (here represented by our “unmixed reference”) to sampling location P2. But, contrary to what
8
9 is observed with the pre-solvent blended composites, the scattering intensity changes very
10
11 little with processing from sampling location P2 to the die outlet.
12
13

14
15 We continued our SANS analysis by determining the slopes of the SANS data in their
16
17 linear regions (between 0.009 and 0.015 Å⁻¹ for the pre-solvent processed composite samples
18
19 compression molded at 90 °C and 170 °C, and between 0.009 and 0.025 Å⁻¹ for the pre-
20
21 solvent processed composite samples collected from the extruder and for the composite
22
23 samples prepared from mixed powders) with a simple power law model fit of the form $I(q) \propto$
24
25 q^{-m} , where m is related to the fractal dimension of the underlying structure.
26
27

28
29 Considering first the samples prepared from pre-solvent processed composites, we find the
30
31 value of m increases from 1.2 at 90 °C, to 1.8 at 170 °C, and to 2.7, 3.1 and 3.3 at sampling
32
33 locations P2, P9 and the extruded ribbon, respectively (see details in Table 2). This indicates
34
35 that with increasing temperature and residence time inside the extruder, the mass distribution
36
37 of C₆₀ changes from something sparsely distributed to something more clustered, with the PS-
38
39 C₆₀ interfaces becoming better defined. These factors point to nano-agglomeration of the C₆₀.
40
41

42
43 Turning now to the composite samples prepared from mixed powders of PS and C₆₀, we
44
45 find that the value of m exhibits a small decrease from 2.6 in P2, 2.5 in P9 and 2.4 in the
46
47 extruded ribbon (Table 2). This indicates that processing induces a slight shift in the C₆₀ mass
48
49 distribution towards something less clustered and with more diffuse PS-C₆₀ interfaces,
50
51 suggesting some improvement of dispersion in these composites.
52
53
54
55
56
57
58
59
60

		$C_{DB} (\text{\AA}^{-4})$	$\Delta\rho (\text{\AA}^{-2})$	Length L (nm)	m
Pre-Solvent Blended	90 °C	$2.5 \times 10^{-6} \pm 2.9 \times 10^{-7}$	3.91×10^{-7}	14.7 ± 4.1	1.2 ± 0.3
	170 °C	$3.9 \times 10^{-6} \pm 1.2 \times 10^{-6}$	4.88×10^{-7}	25.0 ± 12.3	1.8 ± 0.3
	P2	$3.8 \times 10^{-5} \pm 8.4 \times 10^{-7}$	1.52×10^{-6}	20.7 ± 0.8	2.7 ± 0.03
	P9	$7.3 \times 10^{-5} \pm 1.1 \times 10^{-6}$	2.11×10^{-6}	20.5 ± 0.5	3.1 ± 0.02
	Ribbon	$9.7 \times 10^{-5} \pm 2.2 \times 10^{-6}$	2.44×10^{-6}	25.5 ± 0.9	3.3 ± 0.02
From Mixed Powders	P2	$3.2 \times 10^{-5} \pm 3.8 \times 10^{-7}$	1.40×10^{-6}	14.9 ± 0.4	2.6 ± 0.03
	P9	$3.0 \times 10^{-5} \pm 3.9 \times 10^{-7}$	1.35×10^{-6}	15.6 ± 0.5	2.5 ± 0.03
	Ribbon	$2.4 \times 10^{-5} \pm 7.6 \times 10^{-7}$	1.21×10^{-6}	14.9 ± 1.2	2.4 ± 0.07

Table 2. SANS fitting parameters (DAB model) for the q range $0.009 - 0.2545 \text{ \AA}^{-1}$. C_{DB} is the scaling factor, $\Delta\rho$ is the contrast between the two phases, L is the average distance between the two phases and m is the slope of the SANS data in their linear region extracted using the power law model ($I(q) \propto q^{-m}$).

A more quantitative approach to interpreting the SANS data is to model-fit it over its full range ($q = 0.009 - 0.2545 \text{ \AA}^{-1}$). The model we have chosen to use for this is the Debye-Bueche (DB), also called the Debye-Anderson-Brumberger (DAB), model^{44, 45} (Equation 1). This model calculates the scattering from a randomly distributed, two-phase system that is characterized by a single length scale - the correlation length, L - which is a measure of the average spacing between regions of the two different phases (1 and 2). Crucially, this model makes no assumptions about the underlying morphology of the sample. The DAB function has the form

$$I(q) = C_{DB} \frac{L^3}{(1+(qL)^2)^2} + \text{background} \quad (1)$$

where the pre-factor $C_{DB} = 8\pi K(\Delta\rho)^2 \phi_1 \phi_2$, where $\Delta\rho$ is the neutron scattering length density

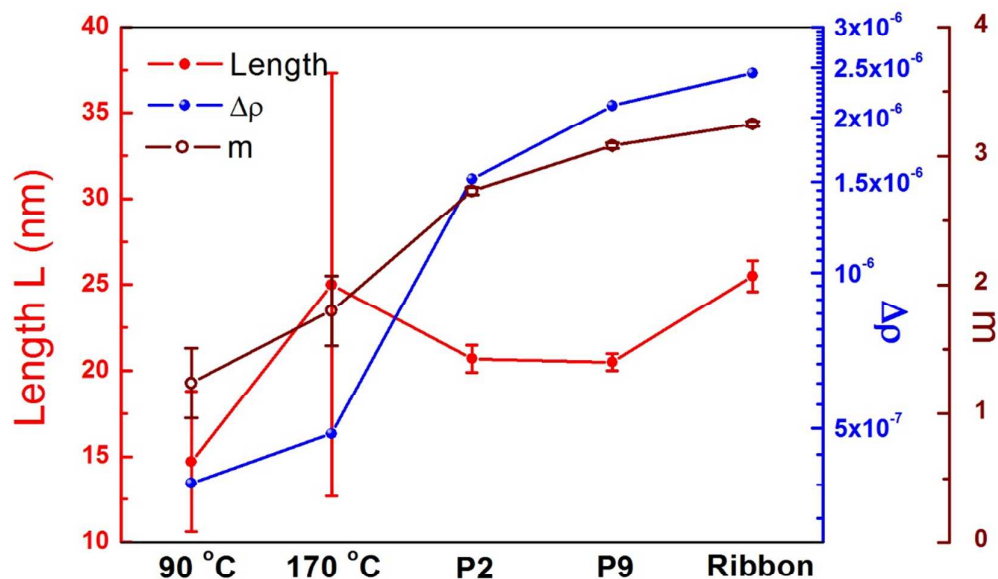
1
2
3 difference between the phases having volume fractions of ϕ_1 and ϕ_2 and K is a scalar to
4
5 convert the units of L^{-1} to those of $I(q)$ (i.e. cm^{-1}).
6
7

8 As shown in Figure 4, the DAB model (solid lines) gives a good description of the data.
9
10 We have not fitted the data for the sample of mixed powders compression molded at 170 °C
11 (sample “mixed powders – initial” in Figure S.I.2 in Supporting Information) and for the
12 extruded ribbon of pure PS because neither of these samples conforms to the physics of the
13 DAB model. The small amount of residual low- q scattering that is evident in these two
14 samples results most likely from some large-scale heterogeneities (e.g., voids).
15
16
17
18
19
20
21

22 The values obtained from the fitting for C_{DB} and L using Equation 1 are shown in Table 2.

23 The values of $\Delta\rho$ calculated from the respective C_{DB} values are also included. All these
24 values are depicted graphically in Figure 5.
25
26
27
28
29

30 (a)



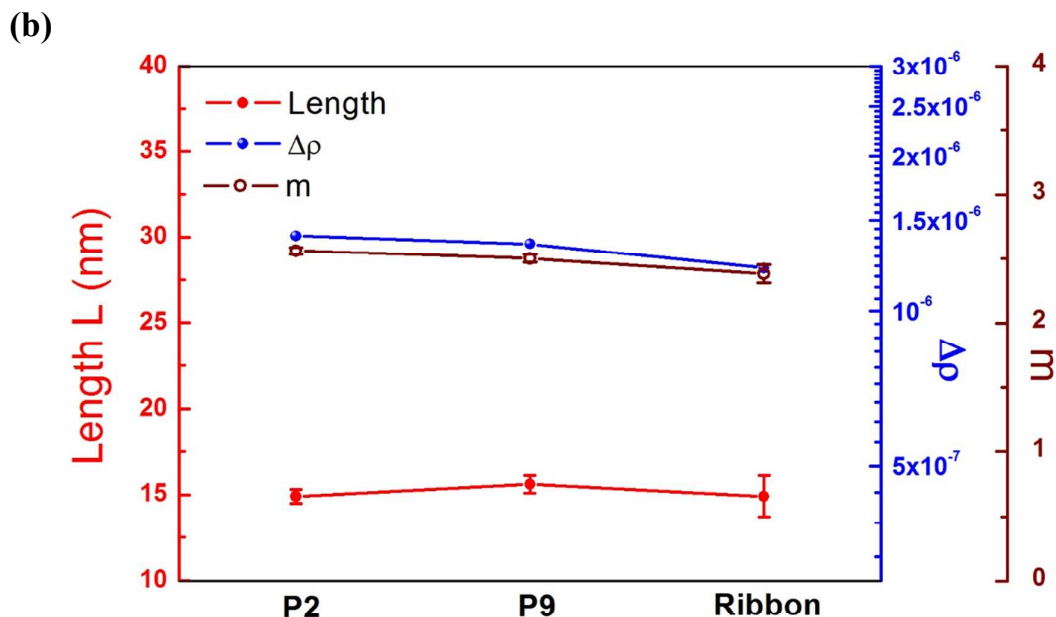


Figure 5. Evolution of the correlation length (L), phase contrast ($\Delta\rho$) and slope (m) with processing for the samples prepared: (a) From pre-solvent-blended composites; (b) From mixed powders of pure PS and pure C_{60} .

According to the values in Figure 5(a) and in Table 2, in the case of the samples prepared from solvent-processed blends, there is some increase in correlation length of the phase domains along the barrel of the extruder which indicates the occurrence of some phase domain coarsening. However, the most striking feature of these samples is the ~ 1 order of magnitude increase in the scattering length density difference between the two phases ($\Delta\rho$), from $3.91 \times 10^{-7} \text{ \AA}^{-2}$ in the initial sample to $2.44 \times 10^{-6} \text{ \AA}^{-2}$ in the extruded ribbon, which clearly indicates that during processing the phases become purer due to C_{60} re-agglomeration. In the extreme situation of having pure phases of PS and pure phases of C_{60} the corresponding $\Delta\rho$ would be $4.19 \times 10^{-6} \text{ \AA}^{-2}$.

According to Figure 5(b) and Table 2, in the case of composite samples prepared from powder mixtures of pure C_{60} and PS, the correlation length between the two phases remains

1
2
3 approximately constant (~ 15 nm) from sample P2 to the extruded ribbon and the phase
4
5 contrast decreases slightly suggesting only a slight improvement in the quality of the nano-
6
7 dispersion.
8
9

10 In summary, therefore, our SANS results show that the major changes in the nano-
11 morphology of the PS-C₆₀ composites occur in the early stages of the extrusion process,
12 between the hopper and sampling port #2. This is in accordance with observations reported
13 for other polymer-based systems, such as polymer blends and composites containing layered
14 silicates, carbon nanotubes or graphene derivatives. As the material reaches the first kneading
15 zone of the screw, it melts as a result of a combination of conducted and dissipated heat.
16 Since melt temperatures are still low, hydrodynamic stresses are high, favouring dispersion.
17 Moreover, flow through kneading disks is complex, promoting distribution. Furthermore,
18 according to our SANS results, in the case of composites prepared from the pre-solvent blend
19 the main morphological evolution that occurs along the extruder is a continuous re-
20 agglomeration of the initially molecularly dispersed C₆₀ into purer phase domains. In the case
21 of composites prepared from mixed powders the main morphological evolution is an initial
22 abrupt increase in the degree of dispersion up to sampling location P2, followed by a much
23 less visible morphological evolution from P2 to the die exit.
24
25
26
27
28
29
30
31
32
33
34
35
36
37
38
39
40

41 Figure 6 illustrates the SAXS data for the same samples as in Figure 4, namely in Figure
42 6(a) for the pre-solvent blended composites heated to 90 °C, 170°C and also collected from
43 P2, P9 and extruded ribbon, and in Figure 6(b) for the composites compounded from mixed
44 powders and collected at P2, P9 and extruded ribbon. Again, data in the q range 0.009 – 0.025
45 \AA^{-1} was fitted with a linear power law and obtained values of m . These are plotted in Figure
46
47
48
49
50
51
52
53
54
55
56
57
58
59
60

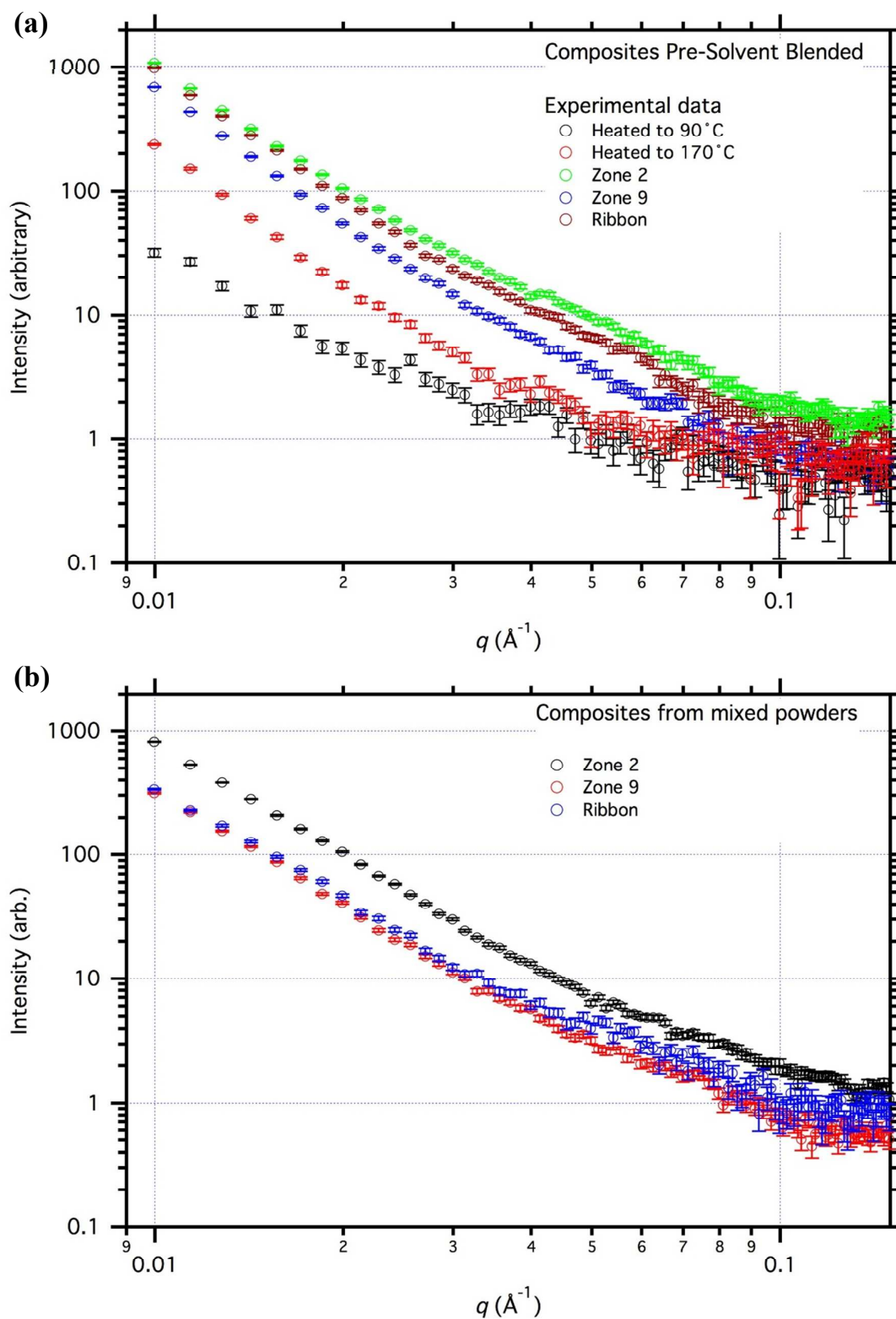


Figure 6. Small angle X-ray scattering of extruded PS and PS-C₆₀ nanocomposites: (a) Pre-solvent blended; (b) Prepared from mixed powders of PS and C₆₀.

1
2
3 As seen, in both Figures 6(a) and 6(b) as well as in Figure S.I.5. in Supporting
4 Information, the SAXS data show trends very similar to those observed in the corresponding
5 SANS data, namely: (a) in the case of pre-solvent blended composites m increases
6 progressively from $m=2.5$ in the sample heated to 90 °C to $m=3.4$ in the extruded ribbon; (b)
7 in the case of composites from mixed powders m changes only very little between sampling
8 location P2 and the extruded ribbon, specifically a small decrease is observed from $m=3.0$ in
9 location P2 to $m=2.9$ in the extruded ribbon. These observations corroborate the previous
10 SANS results showing that: (a) in the case of samples prepared from pre-solvent processed
11 blends, PS-C₆₀ interfaces become progressively sharper as the material progresses along the
12 screw which points strongly to the occurrence of C₆₀ re-agglomeration; (b) in the case of
13 samples prepared from mixed powders, there is a slight improvement in mixing from
14 sampling location P2 to the extruded ribbon with the PS-C₆₀ interfaces becoming slightly less
15 sharp.

16
17
18
19
20
21
22
23
24
25
26
27
28
29
30
31
32 The 1D WAXS patterns for the two samples prepared from the two different feeding
33 formulations and collected from sampling port #P9 are shown in Figure S.I.6. in Supporting
34 Information. In both samples the two broad amorphous halos with maxima at $q = 0.75 \text{ \AA}^{-1}$
35 and $q = 1.35 \text{ \AA}^{-1}$ are due to the amorphous polystyrene. For mixed powders, at location P9 a
36 crystalline C₆₀ peak is clearly visible at $q = 0.77 \text{ \AA}^{-1}$ as well as two small peaks at $q = 1.26$
37 and 1.48 \AA^{-1} ³⁴. These peaks, which are not visible in the pre-solvent processed sample, are
38 due to the presence of crystalline C₆₀ aggregates^{21, 34}. These results reinforce those obtained
39 by O.M. and SESANS showing that extruded samples processed from mixed powders retain
40 crystalline C₆₀ aggregates while the samples processed from pre-solvent blend either do not
41 have any crystalline C₆₀ aggregates or have them in such a low quantity that they are below
42 the detection limit of the WAXS technique.

43
44
45
46
47
48
49
50
51
52
53
54
55
56
57 To investigate this morphological evolution further, we have performed some
58
59
60

1
2
3 Transmission Electron Microscopy (TEM) analysis of the samples collected from P2 and P9
4
5 for both the composites prepared from mixed powders and from pre-solvent blend. Figures
6
7 S.I.7 and S.I.8 in Supporting Information show some representative TEM images. The TEM
8
9 images show that in the case of composites processed from mixed powders the size and
10
11 number of aggregates decreases along the extruder and in the case of composites processed
12
13 from the solvent blend the size and number of the aggregates increases along the extruder, a
14
15 finding in good qualitative agreement with our SANS data.
16
17
18

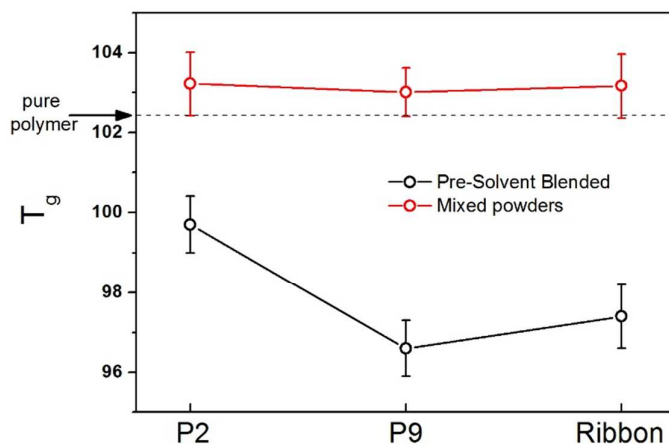
19 Before proceeding further, we believe it is important to make a few comments about the
20
21 complementarity of some of the different direct measurement techniques for assessing
22
23 nanocomposite morphology. Whilst TEM is arguably more accessible than neutron scattering,
24
25 it nonetheless has some drawbacks, particularly for studying polymer composites. First, there
26
27 is the issue of the representative nature of the sampling process: TEM is subjective in the
28
29 sense that the operator must search the sample for regions of interest, and those regions of
30
31 interest must be at, or near to, the surface of the sample. In contrast SANS is a bulk sampling
32
33 technique: the beam is essentially the same size as the sample and the weak neutron-nucleus
34
35 interaction conveys depth penetration. In the present work we have used a 10 mm diameter
36
37 neutron beam, meaning the illuminated area $\sim 78 \text{ mm}^2$ ($= 78,000,000 \text{ }\mu\text{m}^2$). However, in the
38
39 TEM pictures shown in the Supporting Information the maximum area probed in a single
40
41 picture (Figure S.I.7.(a)) is only $\sim 60 \text{ }\mu\text{m}^2$. SAXS suffers from a similar limitation to TEM in
42
43 this respect. Second, to achieve any penetration into a sample with electron or X-ray beams it
44
45 is necessary to use beams of high energy (many keV), energies that are way beyond covalent
46
47 bond energies meaning that there is a significant possibility of radiation-induced damage in
48
49 the sample. The ‘cold’ neutrons used in SANS, on the other hand, have energies of just a few
50
51 meV, meaning SANS is a genuinely non-destructive technique. Lastly, there is the issue of
52
53 phase contrast. Electrons and X-rays interact with atomic electrons meaning that the greatest
54
55
56
57
58
59
60

1
2
3 contrast is obtained between elements of significantly different atomic number. In our
4
5 samples we have carbon dispersed in a matrix of carbon and hydrogen. This means that, for
6
7 example, in the TEM pictures we have provided in the Supporting Information, there is no
8
9 reliable way of knowing if what we see are aggregates of C₆₀ in a matrix of pure PS or
10
11 regions rich in C₆₀ in a soup of PS with some very well molecularly dispersed C₆₀. In SANS,
12
13 however, the phase contrast also stems from the neutron-nucleus interaction and can be very
14
15 different between nuclei of similar atomic number, as it indeed is between carbon and
16
17 hydrogen. Thus, whilst our neutron measurements do not provide the same visually-intuitive
18
19 picture of a sample that TEM does, they are sensitive to structural information that TEM
20
21 simply is not.
22
23
24

25
26 In Figure 7 we show the DSC data, where we plot the variation of the glass transition
27
28 temperature T_g with processing. The T_g of the pure polystyrene is ~102.4 °C. In the case of
29
30 composites processed from mixed powders of C₆₀ and PS we observe that the corresponding
31
32 T_g increases to ~103.2 °C at location P2 and then remains approximately unaltered at P9 and
33
34 in the extruded ribbon. Based on previous work^{19, 32, 34} this ~0.8 °C increase in T_g may be
35
36 explained by the occurrence of some molecular dispersion of C₆₀ in the PS matrix and
37
38 corroborates our SANS results. It also shows that this molecular dispersion principally occurs
39
40 in the first part of the extruder, i.e. between the hopper and sampling location P2. In the case
41
42 of the samples extruded using pre-solvent blended composites we note that the T_g of the
43
44 initial solvent blended powder was ~100°C, i.e. lower than the T_g of the pure polymer. This
45
46 most likely results from the fact that the solvent-blended composite still contained some
47
48 traces of solvent trapped inside the material in spite of the drying under vacuum at 100 °C for
49
50 several hours. In order to probe for the presence of trapped-solvent we have performed some
51
52 thermogravimetric analysis (TGA) of the solvent-blended composites (Figure S.I.9. in
53
54 Supporting Information) which showed no clear evidence of its presence, within the
55
56
57
58
59
60

1
2
3 resolution of the technique. However, we did observe contamination on surface of solvent
4 processed samples caused by the electron beam (Figure S.I.10). This well-known surface
5 contamination is electron beam induced deposition of excess volatile carbonaceous species.
6
7
8
9
10 These observations strongly suggest that trapped-solvent is present in very small amounts,
11
12 although enough to decrease the T_g of the system by several degrees Celsius.
13

14
15 The most interesting feature of the T_g of the solvent-blended composites, is that it drops
16 from ~ 99.7 °C to ~ 96.6 °C respectively at P2 and P9 and then it remains approximately
17 constant between P9 and the extruded ribbon. Based also on previous work^{19, 32, 34}, this
18 decrease in T_g along the extruder is most likely due to the fact that C_{60} is leaving the PS
19 matrix and re-agglomerating, as also supported by our SANS results.
20
21
22
23
24
25
26
27



28
29
30
31
32
33
34
35
36
37
38
39
40
41
42
43
44
45
46
47
48
49
50
Figure 7. Variation of the glass transition temperature (T_g) along processing. T_g was
determined using the extrapolated half- C_p method. Associated error bars are typically $<$
 ± 1 °C.

51
52
53
54
55
56
57
58
59
60
Figure 8 shows the mechanical spectra of the PS matrix and the composites obtained when
processing the pre-solvent blended composites (a) or the mixed powders (b).

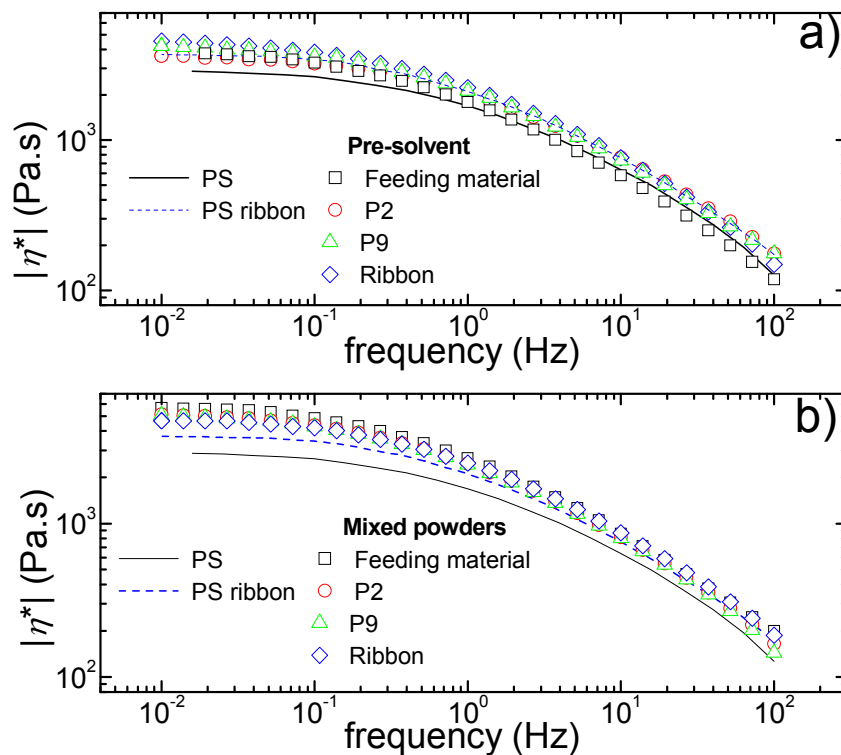


Figure 8. Frequency dependence of the dynamic viscosity $|\eta^*|$ for the matrix (lines), the solvent prepared composite (a) and the mixed powders composite (b) all measured at different locations along the extruder.

Rheological data of PS samples collected along the extruder first reveal that the PS matrix is sensitive to processing. The PS ribbon spectrum is shifted to larger viscosity values for all frequencies with respect to the PS powder sample. Thermo-oxidative crosslinking reported recently for a PS nanocomposite⁴⁶ could explain the increase in the zero shear viscosity of PS ribbon samples. This degradation process is further supported by the rheological data presented in Figure S.I.11. (in Supporting Information), where a gradual increase in the zero shear viscosity of PS samples collected along the extrusion line relates with the increasing residence time of each sample in the extruder.

Although entanglements in the PS matrix are evident in the master curve (see Figure S.I.12. in Supporting Information which shows a rubbery plateau prior to the glass transition regime), no reduction in the zero shear viscosity of the PS nanocomposite produced with the

1
2
3 solvent method is seen in Figure 8(a). Thus the non-Einstein behavior reported elsewhere for
4 a similar system^{16, 47} and for other well dispersed polymer nanocomposites^{46, 48} is not
5 reproduced here. The C₆₀ dispersion quality required to produce a viscosity reduction is not
6 met in the powder sample produced with the solvent method. Indeed SANS indicated that the
7 minimum distance between aggregates is of the order of 15 nm in this sample, which is much
8 larger than the size of the PS chain. This poor molecular dispersion of C₆₀ therefore explains
9 the reinforcement of the PS matrix mirrored in the enhanced viscoelasticity for all
10 frequencies.
11
12
13
14
15
16
17
18
19

20
21 The melt processing of the solvent based PS composite is accompanied with an increase in
22 the dynamic viscosity. Indeed, the progressive increase from P2 to P9 does partially correlate
23 with the viscosity increase of the thermally degraded matrix, as demonstrated by the constant
24 viscosity ratio between composite and matrix which nearly matches an Einstein like value
25 between P2 and P9 (see Figure S.I.13. in Supporting Information).
26
27
28
29
30
31

32
33 However, the breakdown of Einstein like behavior for the powder sample is concomitant
34 with the presence of structural heterogeneities below 20 nm in the solvent based PS
35 composite which impedes the interpretation of the rheological data using classical continuum
36 theories¹¹. Overall, rheological changes along the processing of the solvent based feeding
37 formulation are in harmony with the re-agglomeration process (SANS and TEM data both
38 showing a coarsening of the structure along the extruder) which progressively leads to an
39 Einstein-like reinforcement of the PS matrix.
40
41
42
43
44
45
46
47

48
49 The situation is changed for the mixed powders as the Newtonian viscosity in Figure 8(b)
50 shows a monotonic decrease along the extruder. In contrast to this, the high frequency regime
51 of the dynamic viscosity is not sensitive to the residence time in the extruder nor to the
52 progressive structural rearrangement. Thus, the process-induced reduction in C₆₀ aggregates
53 size does not impact on the entanglement plateau, whereas it accelerates the terminal
54
55
56
57
58
59
60

1
2
3 relaxation time of the PS matrix. Similar effects were reported in well dispersed PS
4 nanocomposites containing dendritic polyethylene particles ⁴⁶ or PS nanoparticles ⁴⁹.
5
6
7 Confinement of PS chain together with additional free volume brought by the nanoparticles
8 were called for explaining the non-classical viscosity reduction in the latter system, whereas
9 such effects were ruled out for the former polymer nanocomposite. Although local chain
10 confinement cannot be excluded (the SANS analysis suggests an aggregate-aggregate
11 distance of the order of 15 nm), the existence of large aggregates in microscopic imaging
12 supports the larger viscosity and slower dynamics of the mixed powders when compared to
13 the neat PS.
14
15
16
17
18
19
20
21
22

23
24 Rationalizing the zero shear viscosities of the composites and the PS matrix shows that
25 after P9, no evolution is observed in the rheology of the processed mixed powders. This is in
26 contrast to the viscosity increase from P9 to the extrudate observed with the solvent route,
27 which eventually results in a close matching between the rheological properties of the two
28 extrudates (see Figure S.I.14. in Supporting Information).
29
30
31
32
33
34

35 Thus, this rheological similarity suggests a dynamically equivalent macroscopic
36 morphology for the two types of composite extrudates. However, the routes for achieving
37 similar viscosity levels are different, as the re-agglomeration of the solvent based feeding
38 formulation opposes to the break-up/erosion of aggregates and molecular dispersion of C₆₀ in
39 the composites from mixed powders.
40
41
42
43
44
45

46 The relative sizes of PS chains and aggregates, the dynamics of the polymer close to the
47 aggregates, the interfacial tensions, the aggregates-aggregates interactions and C₆₀-PS
48 interactions all contribute in a complex fashion to the rheology of these composites. Because
49 the interplay between rheology and all these ingredients is far from being understood even in
50 model systems ⁵⁰, the rheological data collected in Figure 8 essentially indicate that for the
51
52
53
54
55
56
57
58
59
60

1
2
3 present PS-C₆₀ composite, the re-agglomeration process gives way to an increase in the
4
5 dynamic viscosity, whereas the structural sizing down corresponds to reduced viscosity.
6
7

8 9 **4. Conclusions**

10
11
12 In this work we studied the effect of the initial feeding formulation on the morphology
13 evolution of PS-C₆₀ nanocomposites along the axis of a twin screw extruder. Two markedly
14 different initial feed formulations comprising 1 wt% C₆₀ were used, namely: (a) a simple
15 mechanical mixture of PS and C₆₀ powders and (b) a PS-C₆₀ composite prepared by solvent
16 blending. The study was carried out by performing sequential sampling along the extruder
17 and by characterizing the corresponding degrees of dispersion. A number of experimental
18 techniques were used to probe the dispersion levels at different length scales, namely: optical
19 microscopy, spin-echo small angle neutron scattering (SESANS), small angle neutron
20 scattering (SANS), small angle x-ray scattering (SAXS) and wide-angle x-ray scattering
21 (WAXS). These are complemented by differential scanning calorimetry (DSC) and
22 rheological measurements.
23
24
25
26
27
28
29
30
31
32
33
34
35

36
37 According to our results, the vastly different morphologies of the initial feeding
38 formulations (situation A for mixed powders and situation D for the solvent blend, in Figure
39 1) converge along the extruder into a similar final nanomorphology (situation C in Figure 1)
40 which strongly suggests that the final morphology is mainly dictated by the coupling between
41 thermodynamics and flow leading to a preferred steady state of the system which is
42 independent of the initial conditions.
43
44
45
46
47
48
49

50
51 Furthermore, this work strongly suggests that starting from a perfectly solvent-blended
52 mixed system and promoting its re-agglomeration along the extruder might be a good
53 strategy to prepare nanocomposites when some level of particle aggregation is advantageous
54 to specific applications^{10, 11}.
55
56
57
58
59
60

Acknowledgments

This work was funded by FEDER funds through the COMPETE 2020 Program and National Funds through FCT - Portuguese Foundation for Science and Technology under the project UID/CTM/50025/2013. Funding from FEDER through the program COMPETE (Project EXPL/CTM-POL/0933/2012) is also acknowledged.

SANS data were collected during beam time provided through the user program at the ISIS Neutron and Muon Source, operated by the UK Science & Technology Facilities Council.

We thank Chris Duif (TU Delft) for assistance with the SESANS measurements.

This work benefited from DANSE software developed under NSF award DMR-0520547.

Author Contributions

G.B., J.A.C. and L.H. originated the initial experimental and overall motivation for the work. L.F. prepared the solvent-blended composite. H.G. and P.T. performed the extrusion experiments. R.S. undertook the optical microscopy characterization. W.G.B. and S.R.P. conducted the Spin-Echo-SANS characterization. G.B., S.M.K., A.J.P. and N.C. performed the SANS measurements and analysis. M.W. and N.C. carried out the SAXS measurements and analysis. A.J.P. undertook the WAXS analysis. G.B. and H.G. performed the DSC characterization. L.H., P.T. and H.G. performed the rheological characterization. C.J.H. undertook the TEM analysis. K.J.A. carried out the STEM characterization. G.B. performed the TGA study. G.B. wrote the initial draft of the manuscript with inputs from all the authors and subsequently the draft was revised by all the authors.

References

1. Verdejo, R.; Bernal, M. M.; Romasanta, L. J.; Lopez-Manchado, M. A. Graphene filled polymer nanocomposites. *Journal of Materials Chemistry* **2011**, 21 (10), 3301-3310
2. Cai, D.; Song, M. Recent advance in functionalized graphene/polymer nanocomposites. *Journal of Materials Chemistry* **2010**, 20 (37), 7906-7915
3. Sahoo, N. G.; Rana, S.; Cho, J. W.; Li, L.; Chan, S. H. Polymer nanocomposites based on functionalized carbon nanotubes. *Progress in Polymer Science* **2010**, 35 (7), 837-867
4. Karatrantos, A.; Composto, R. J.; Winey, K. I.; Clarke, N. Structure and Conformations of Polymer/SWCNT Nanocomposites. *Macromolecules* **2011**, 44 (24), 9830-9838
5. Tung, W. S.; Bird, V.; Composto, R. J.; Clarke, N.; Winey, K. I. Polymer Chain Conformations in CNT/PS Nanocomposites from Small Angle Neutron Scattering. *Macromolecules* **2013**, 46 (13), 5345-5354
6. Tung, W. S.; Composto, R. J.; Clarke, N.; Winey, K. I. Anisotropic Polymer Conformations in Aligned SWCNT/PS Nanocomposites. *Acs Macro Letters* **2015**, 4 (9), 916-920
7. Kota, A. K.; Cipriano, B. H.; Duesterberg, M. K.; Gershon, A. L.; Powell, D.; Raghavan, S. R.; Bruck, H. A. Electrical and rheological percolation in polystyrene/MWCNT nanocomposites. *Macromolecules* **2007**, 40 (20), 7400-7406
8. Badamshina, E.; Gafurova, M. Polymeric nanocomposites containing non-covalently bonded fullerene C-60: properties and applications. *Journal of Materials Chemistry* **2012**, 22 (19), 9427-9438

- 1
2
3 9. Karatrantos, A.; Clarke, N.; Kröger, M. Modeling of Polymer Structure and
4 Conformations in Polymer Nanocomposites from Atomistic to Mesoscale: A Review.
5 *Polymer Reviews* **2016**, 56 (3), 385-428
6
7
8
9
10 10. Balazs, A. C.; Emrick, T.; Russell, T. P. Nanoparticle polymer composites: Where
11 two small worlds meet. *Science* **2006**, 314 (5802), 1107-1110
12
13
14 11. Jancar, J.; Douglas, J. F.; Starr, F. W.; Kumar, S. K.; Cassagnau, P.; Lesser, A. J.;
15 Sternstein, S. S.; Buehler, M. J. Current issues in research on structure-property relationships
16 in polymer nanocomposites. *Polymer* **2010**, 51 (15), 3321-3343
17
18
19
20
21 12. Scurati, A.; Feke, D. L.; Manas-Zloczower, I. Analysis of the kinetics of agglomerate
22 erosion in simple shear flows. *Chemical Engineering Science* **2005**, 60 (23), 6564-6573
23
24
25 13. Domingues, N.; Gaspar-Cunha, A.; Covas, J. A.; Camesasca, M.; Kaufman, M.;
26 Manas-Zloczower, I. Dynamics of Filler Size and Spatial Distribution in a Plasticating Single
27 Screw Extruder - Modeling and Experimental Observations. *International Polymer*
28 *Processing* **2010**, 25 (3), 188-198
29
30
31
32
33
34 14. Hedberg, K.; Hedberg, L.; Bethune, D. S.; Brown, C. A.; Dorn, H. C.; Johnson, R. D.;
35 Devries, M. Bond Lengths in Free Molecules of Buckminsterfullerene, C₆₀, From Gas-Phase
36 Electron-Diffraction. *Science* **1991**, 254 (5030), 410-412
37
38
39
40
41 15. Mu, M.; Seitz, M. E.; Clarke, N.; Composto, R. J.; Winey, K. I. Polymer Tracer
42 Diffusion Exhibits a Minimum in Nanocomposites Containing Spherical Nanoparticles.
43 *Macromolecules* **2011**, 44 (2), 191-193
44
45
46
47 16. Tuteja, A.; Duxbury, P. M.; Mackay, M. E. Multifunctional nanocomposites with
48 reduced viscosity. *Macromolecules* **2007**, 40 (26), 9427-9434
49
50
51
52 17. Kropka, J. M.; Sakai, V. G.; Green, P. F. Local polymer dynamics in polymer-C-60
53 mixtures. *Nano Letters* **2008**, 8 (4), 1061-1065
54
55
56
57
58
59
60

- 1
2
3 18. Vogiatzis, G. G.; Theodorou, D. N. Local Segmental Dynamics and Stresses in
4 Polystyrene-C-60 Mixtures. *Macromolecules* **2014**, 47 (1), 387-404
5
6
7 19. Wong, H. C.; Sanz, A.; Douglas, J. F.; Cabral, J. T. Glass formation and stability of
8 polystyrene-fullerene nanocomposites. *Journal of Molecular Liquids* **2010**, 153 (1), 79-87
9
10
11 20. Bernardo, G.; Deb, N.; King, S. M.; Bucknall, D. G. Phase behavior of blends of
12 PCBM with amorphous polymers with different aromaticity. *Journal of Polymer Science Part*
13 *B: Polymer Physics* **2016**, 54 (10), 994-1001
14
15
16
17 21. Campbell, K.; Gurun, B.; Sumpter, B. G.; Thio, Y. S.; Bucknall, D. G. Role of
18 Conformation in pi-pi Interactions and Polymer/Fullerene Miscibility. *Journal of Physical*
19 *Chemistry B* **2011**, 115 (29), 8989-8995
20
21
22
23 22. Perrin, L.; Nourdine, A.; Planes, E.; Carrot, C.; Alberola, N.; Flandin, L. Fullerene-
24 based processable polymers as plausible acceptors in photovoltaic applications. *Journal of*
25 *Polymer Science Part B-Polymer Physics* **2013**, 51 (4), 291-302
26
27
28
29 23. Chakraborty, C.; Malik, S.; Guenet, J.-M. Syndiotactic Polystyrene/Fullerene
30 Composites: Elucidation of Structural Aspect. *Polymer-Solvent Complexes and Intercalates -*
31 *Polysolvat 8* **2011**, 303
32
33
34
35 24. Troitskii, B. B.; Troitskaya, L. S.; Dmitriev, A. A.; Yakhnov, A. S. Inhibition of
36 thermo-oxidative degradation of poly(methyl methacrylate) and polystyrene by C60.
37 *European Polymer Journal* **2000**, 36 (5), 1073-1084
38
39
40
41 25. Zeinalov, E. B.; Kossmehl, G. Fullerene C-60 as an antioxidant for polymers.
42 *Polymer Degradation and Stability* **2001**, 71 (2), 197-202
43
44
45
46 26. Fernandes, L.; Gaspar, H.; Bernardo, G. Inhibition of thermal degradation of
47 polystyrene by C-60 and PCBM: A comparative study. *Polymer Testing* **2014**, 40, 63-69
48
49
50
51
52
53
54
55
56
57
58
59
60

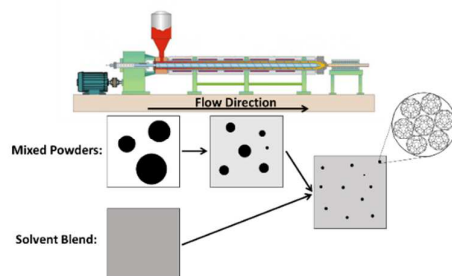
- 1
2
3 27. Pereira, P.; Gaspar, H.; Fernandes, L.; Bernardo, G. Impact of fullerenes on the
4 thermal stability of melt processed polystyrene and poly(methyl methacrylate) composites.
5
6
7 *Polymer Testing* **2015**, 47, 130-136
8
9
10 28. Higuchi, A.; Agatsuma, T.; Uemiya, S.; Kojima, T.; Mizoguchi, K.; Pinnau, I.; Nagai,
11 K.; Freeman, B. D. Preparation and gas permeation of immobilized fullerene membranes.
12
13 *Journal of Applied Polymer Science* **2000**, 77 (3), 529-537
14
15
16 29. Hanson, B.; Pryamitsyn, V.; Ganesan, V. Computer Simulations of Gas Diffusion in
17 Polystyrene-C-60 Fullerene Nanocomposites Using Trajectory Extending Kinetic Monte
18 Carlo Method. *Journal of Physical Chemistry B* **2012**, 116 (1), 95-103
19
20
21
22 30. Han, J. T.; Lee, G.-W.; Kim, S.; Lee, H.-J.; Douglas, J. F.; Karim, A. Direct
23 observation of interfacial C-60 cluster formation in polystyrene-C-60 nanocomposite films.
24
25
26
27 *Nanotechnology* **2009**, 20 (10), 105705
28
29
30 31. Alekseeva, O. V.; Barannikov, V. P.; Bagrovskaya, N. A.; Noskov, A. V. DSC
31 investigation of the polystyrene films filled with fullerene. *Journal of Thermal Analysis and*
32
33
34 *Calorimetry* **2012**, 109 (2), 1033-1038
35
36
37 32. Weng, D.; Lee, H. K.; Levon, K.; Mao, J.; Scrivens, W. A.; Stephens, E. B.; Tour, J.
38 M. The influence of Buckminsterfullerenes and their derivatives on polymer properties.
39
40
41 *European Polymer Journal* **1999**, 35 (5), 867-878
42
43
44 33. Dattani, R.; Cabral, J. T. Polymer fullerene solution phase behaviour and film
45 formation pathways. *Soft Matter* **2015**, 11 (16), 3125-3131
46
47
48 34. Sanz, A.; Wong, H. C.; Nedoma, A. J.; Douglas, J. F.; Cabral, J. T. Influence of C-60
49 fullerenes on the glass formation of polystyrene. *Polymer* **2015**, 68, 47-56
50
51
52 35. Rekveldt, M. T.; Plomp, J.; Bouwman, W. G.; Kraan, W. H.; Grigoriev, S.; Blaauw,
53 M. Spin-echo small angle neutron scattering in Delft. *Review of Scientific Instruments* **2005**,
54
55
56 76 (3), 033901
57
58
59
60

- 1
2
3 36. Londono, J. D.; Narten, A. H.; Wignall, G. D.; Honnell, K. G.; Hsieh, E. T.; Johnson,
4 T. W.; Bates, F. S. Composition Dependence of the Interaction Parameter in Isotopic Polymer
5 Blends. *Macromolecules* **1994**, 27 (10), 2864-2871
6
7
8
9
10 37. Novais, R. M.; Covas, J. A.; Paiva, M. C. The effect of flow type and chemical
11 functionalization on the dispersion of carbon nanofiber agglomerates in polypropylene.
12 *Composites Part a-Applied Science and Manufacturing* **2012**, 43 (6), 833-841
13
14
15
16 38. Machado, A. V.; Covas, J. A.; van Duin, M. Evolution of morphology and of
17 chemical conversion along the screw in a corotating twin-screw extruder. *Journal of Applied*
18 *Polymer Science* **1999**, 71 (1), 135-141
19
20
21
22
23 39. Akeroyd, F.; Ansell, S.; Antony, S.; Arnold, O.; Bekasovs, A.; Bilheux, J.;
24 Borreguero, J.; Brown, K.; Buts, A.; Campbell, S.; Champion, D.; Chapon, L.; Clarke, M.;
25 Cottrell, S.; Dalglish, R.; Dillow, D.; Doucet, M.; Draper, N.; Fowler, R.; Gigg, M. A.;
26 Granroth, G.; Hagen, M.; Heller, W.; Hillier, A.; Howells, S.; Jackson, S.; Kachere, D.;
27 Koennecke, M.; Le Bourlot, C.; Leal, R.; Lynch, V.; Manuel, P.; Markvardsen, A.;
28 McGreevy, R.; Mikkelsen, D.; Mikkelsen, R.; Miller, R.; Nagella, S.; Nielsen, T.; Palmen,
29 K.; Parker, P. G.; Pascal, M.; Passos, G.; Perring, T.; Peterson, P. F.; Pratt, F.; Proffen, T.;
30 Radaelli, P.; Rainey, J.; Ren, S.; Reuter, M.; Sastry, L.; Savici, A.; Taylor, J.; Taylor, R. J.;
31 Thomas, M.; Tolchenov, R.; Whitley, R.; Whitty, M.; Williams, S.; Zhou, W.; Zikovsky, J.
32 Mantid: Manipulation and Analysis Toolkit for Instrument Data.
33 <http://dx.doi.org/10.5286/SOFTWARE/MANTID> (Date of access: 20/07/2016),
34
35
36
37
38
39
40
41
42
43
44
45
46
47 40. Alina, G.; Butler, P.; Cho, J.; Doucet, M.; Kienzle, P. SasView.
48 <http://www.sasview.org/> (Date of access: 20/07/2016),
49
50
51
52 41. Alig, I.; Poetschke, P.; Lellinger, D.; Skipa, T.; Pegel, S.; Kasaliwal, G. R.; Villmow,
53 T. Establishment, morphology and properties of carbon nanotube networks in polymer melts.
54 *Polymer* **2012**, 53 (1), 4-28
55
56
57
58
59
60

- 1
2
3 42. Vilaverde, C.; Santos, R. M.; Paiva, M. C.; Covas, J. A. Dispersion and re-
4 agglomeration of graphite nanoplates in polypropylene melts under controlled flow
5 conditions. *Composites Part a-Applied Science and Manufacturing* **2015**, 78, 143-151
6
7
8
9
10 43. Andersson, R.; van Heijkamp, L. F.; de Schepper, I. M.; Bouwman, W. G. Analysis of
11 spin-echo small-angle neutron scattering measurements. *Journal of Applied Crystallography*
12 **2008**, 41 (5), 868-885
13
14
15
16 44. Debye, P.; Bueche, A. M. Scattering by an Inhomogeneous Solid. *Journal of Applied*
17 *Physics* **1949**, 20 (6), 518-525
18
19
20
21 45. Debye, P.; Anderson, H. R.; Brumberger, H. Scattering by an Inhomogeneous Solid
22 .2. The Correlation Function and its Application. *Journal of Applied Physics* **1957**, 28 (6),
23 679-683
24
25
26
27 46. Goldansaz, H.; Goharpey, F.; Afshar-Taromi, F.; Kim, I.; Stadler, F. J.; van
28 Ruymbeke, E.; Karimkhani, V. Anomalous Rheological Behavior of Dendritic
29 Nanoparticle/Linear Polymer Nanocomposites. *Macromolecules* **2015**, 48 (10), 3368-3375
30
31
32
33
34 47. Mackay, M. E.; Dao, T. T.; Tuteja, A.; Ho, D. L.; Van Horn, B.; Kim, H. C.; Hawker,
35 C. J. Nanoscale effects leading to non-Einstein-like decrease in viscosity. *Nature Materials*
36 **2003**, 2 (11), 762-766
37
38
39
40 48. Nusser, K.; Schneider, G. J.; Pyckhout-Hintzen, W.; Richter, D. Viscosity Decrease
41 and Reinforcement in Polymer-Silsesquioxane Composites. *Macromolecules* **2011**, 44 (19),
42 7820-7830
43
44
45
46
47 49. Tuteja, A.; Mackay, M. E.; Hawker, C. J.; Van Horn, B. Effect of ideal, organic
48 nanoparticles on the flow properties of linear polymers: Non-Einstein-like behavior.
49 *Macromolecules* **2005**, 38 (19), 8000-8011
50
51
52
53
54 50. Song, Y.; Zheng, Q. Linear rheology of nanofilled polymers. *Journal of Rheology*
55 **2015**, 59 (1), 155-191
56
57
58
59
60

1
2
3
4
5
6
7
8
9
10
11
12
13
14
15
16
17 **A Journey Along the Extruder with Polystyrene:C₆₀ Nanocomposites: Convergence of**
18 **Feeding Formulations into a Similar Nano-Morphology**
19

20 Hugo Gaspar, Paulo Teixeira, Raquel Santos, Liliana Fernandes, Loic Hilliou, Michael P.
21 Weir, Andrew J. Parnell, Kerry J. Abrams, Christopher J. Hill, Wim G. Bouwman, Steven R.
22 Parnell, Stephen M. King, Nigel Clarke, José A. Covas, Gabriel Bernardo
23
24
25
26
27
28
29



Supporting Information

A Journey Along the Extruder with Polystyrene:C₆₀ Nanocomposites: Effect of Feeding Formulation on Dispersion and Re-Agglomeration Phenomena

Hugo Gaspar¹, Paulo Teixeira¹, Raquel Santos¹, Liliana Fernandes¹, Loic Hilliou¹, Michael P. Weir², Andrew J. Parnell², Kerry J. Abrams³, Christopher J. Hill⁴, Wim G. Bouwman⁵, Steven R. Parnell⁵, Stephen M. King⁶, Nigel Clarke², José A. Covas^{1,*}, Gabriel Bernardo^{1,*}

¹Institute for Polymers and Composites/I3N, University of Minho, 4800-058 Guimarães, Portugal

²Department of Physics and Astronomy, The University of Sheffield, Sheffield S3 7RH, United Kingdom

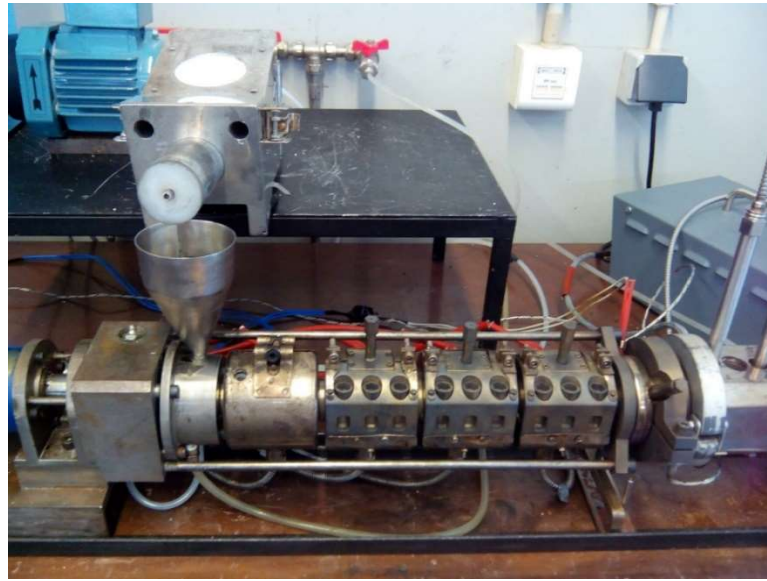
³Department of Materials Science and Engineering, The University of Sheffield, Sheffield S1 3JD, United Kingdom

⁴Department of Biomedical Science, The University of Sheffield, Sheffield S3 7HF, United Kingdom

⁵Faculty of Applied Sciences, Delft University of Technology, Mekelweg 15, 2629 JB Delft, Netherlands

⁶ISIS Pulsed Neutron Source, STFC Rutherford Appleton Laboratory, Harwell Campus, Didcot, OX11 0QX, United Kingdom

(a)



(b)

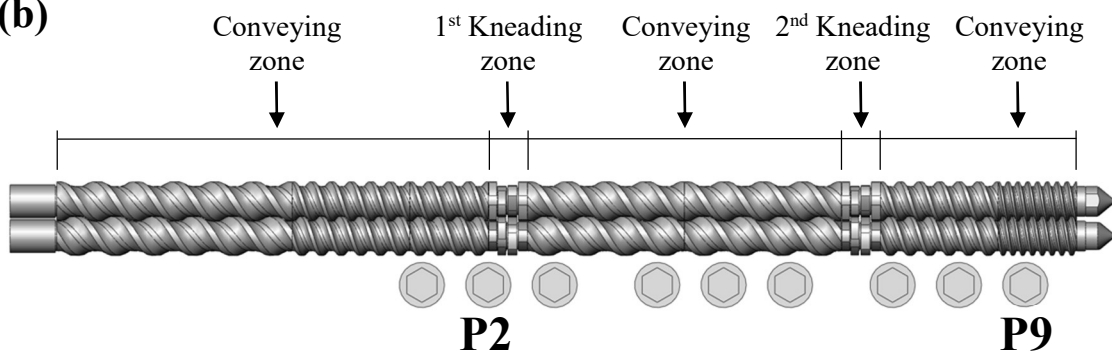


Figure S.I.1. (a) Prototype twin-screw extruder with sampling ports and volumetric feeder; (b) geometry of the screws and identification of the sampling locations P2 and P9.

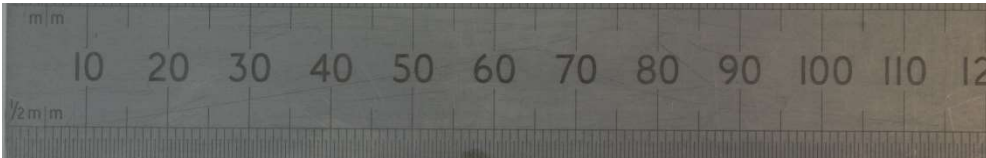








(a)	Initial	P2	P9	Ribbon
				
Mixed Powders				
Pre-Solvent Blended				



Figure S.I.2. (a) Close-up photo of the experimental samples, namely: compression moulded samples of the initial feeding formulations; extruded samples P2; extruded samples P9 and extruded ribbons. A ruler is also shown to indicate the real dimension of the samples.; (b) Close-up photo of the pre-solvent blended initial sample (compression molded at 170 °C), lit from the back to highlight its purple colour.

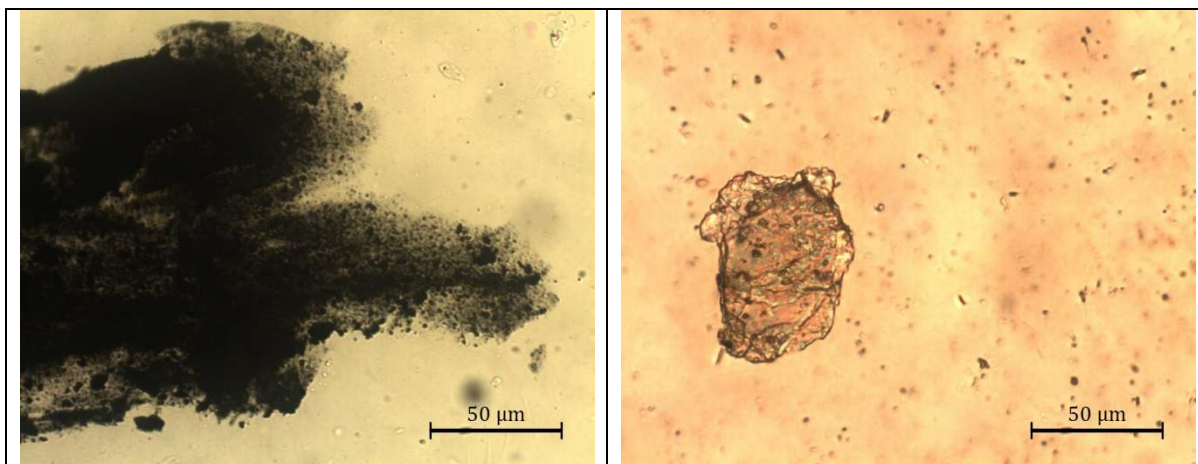
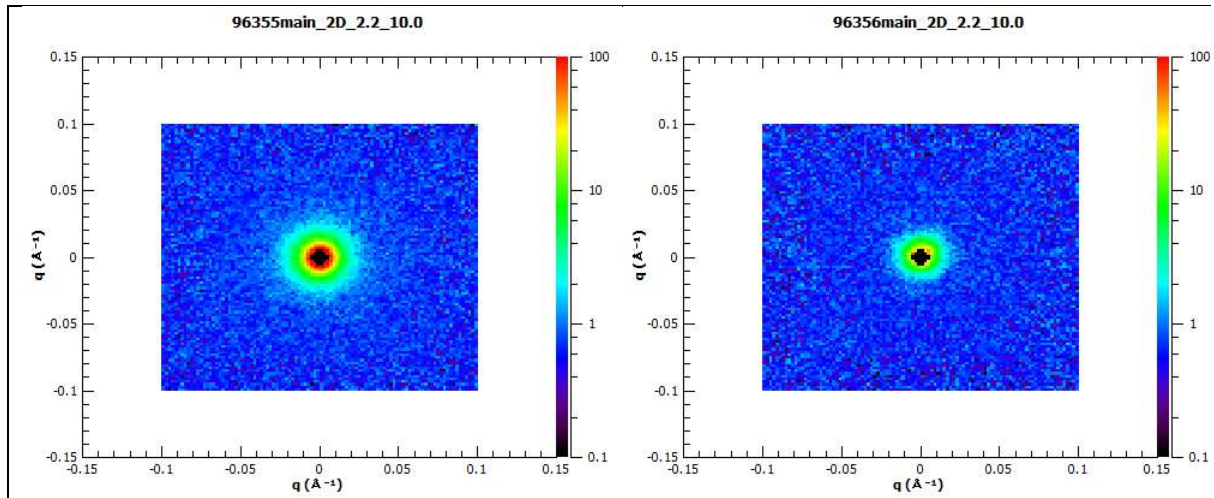


Figure S.I.3. Optical microscopy images of the initial feeding formulations: (left) mixed powders; (right) solvent blended composite. For obtaining these microscopy images, the initial feeding formulations (in powder form) were softened at 160 °C and spread onto a glass slide. The larger, approximately circular, feature with ~50 μm diameter in the image on the right corresponds to material that did not melt during the preparation of the optical microscopy sample.

(a)



(b)

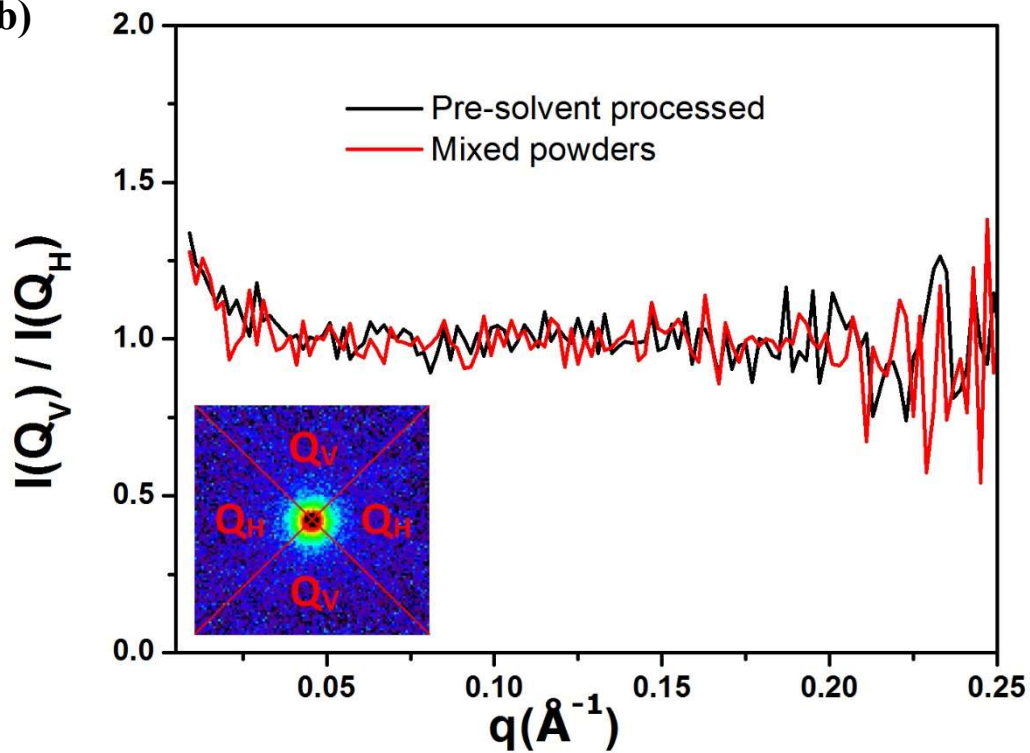


Figure S.I.4. (a) Neutron scattering 2D patterns of extruded ribbons processed from a pre-solvent blend (left) and from mixed powders (right); (b) Intensity ratio $I(Q_V)/I(Q_H)$ as a function of q , for the vertical and horizontal quadrants of the 2D scattering patterns (see inset). The average ratio is ~ 1 which means that the samples are completely isotropic.

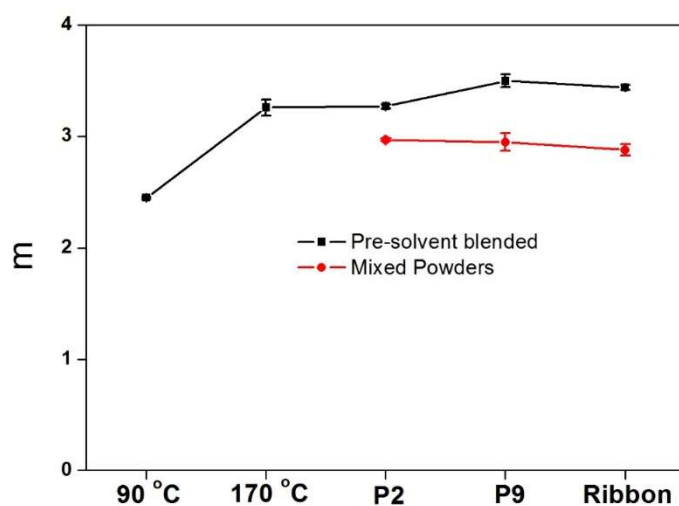


Figure S.I.5. Variation of the slope of the SAXS curves with processing. For ease of comparison the scale used is identical to the scale in Figure 5.

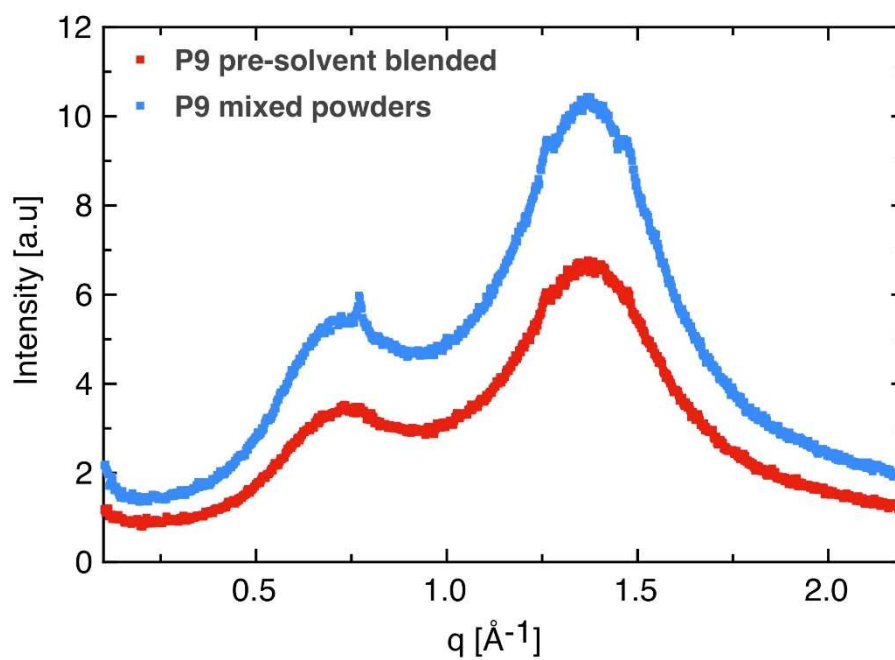


Figure S.I.6. 1D WAXS patterns of samples collected from sampling port #9. The data has been translated vertically for clarity.

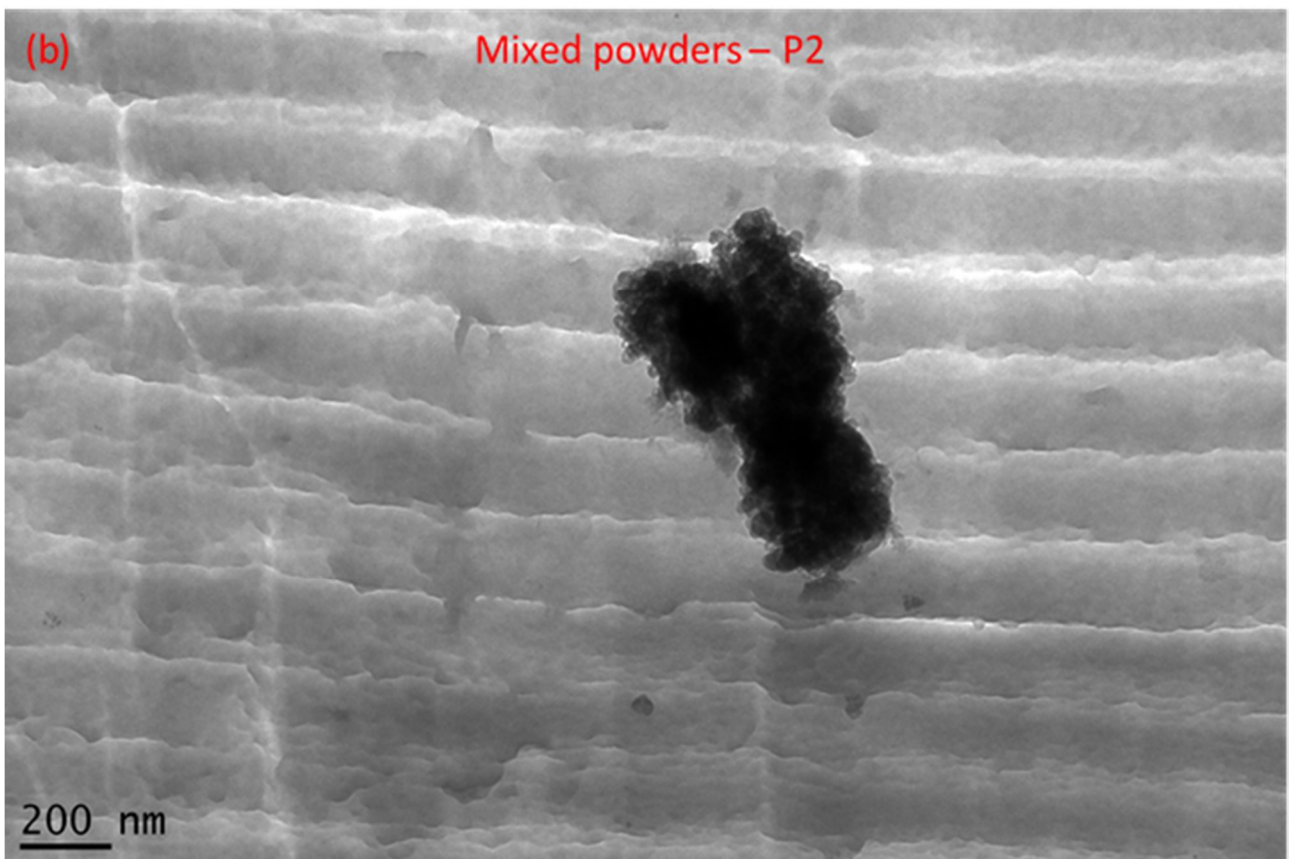
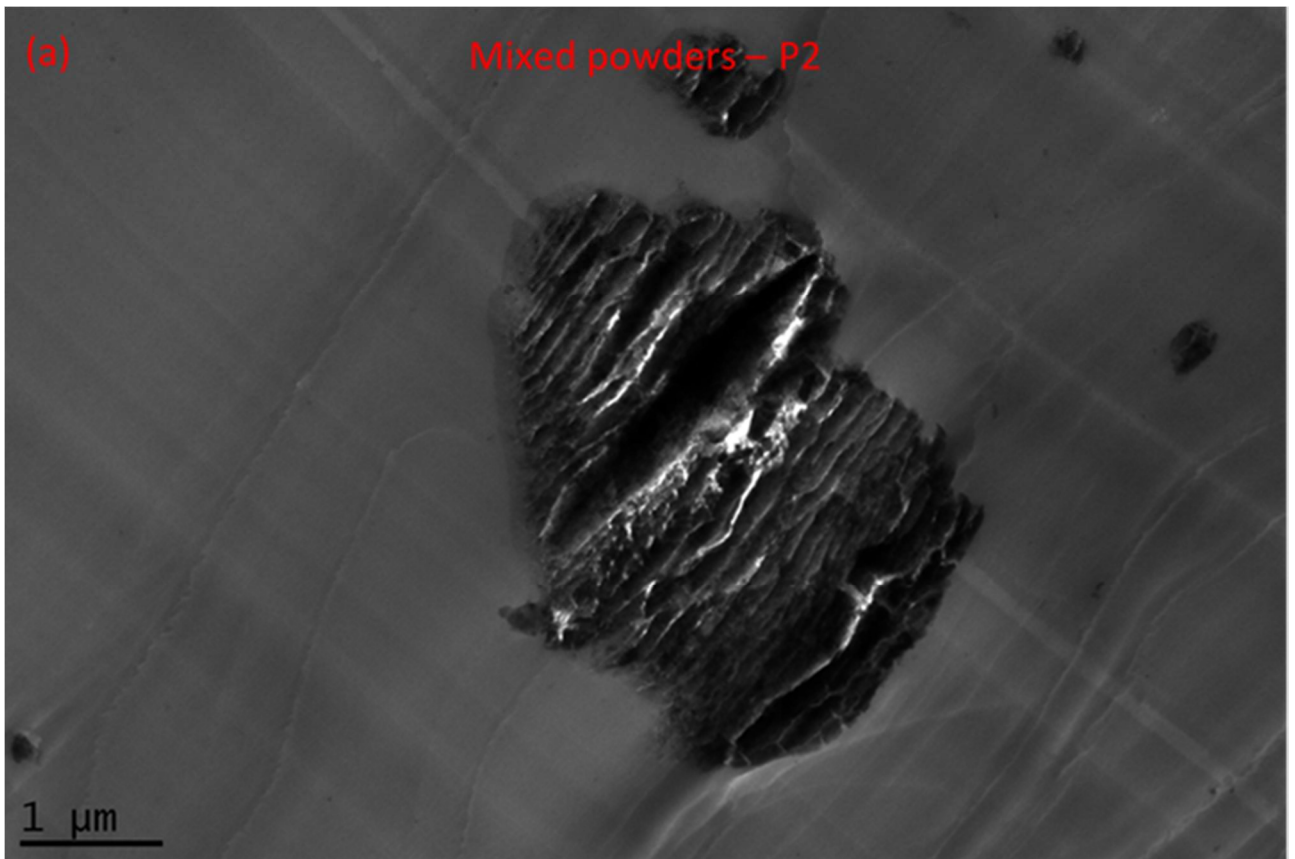
Experimental Procedure for the TEM characterization

Samples were snap frozen in Liquid Nitrogen and placed in the FC6 cryo-chamber to equilibrate for approximately 30 minutes. Ultrathin sections, approximately 90-100nm thick, were cut using a Leica UC 6 ultra-microtome and FC6 cryobox attachment onto uncoated 200 mesh copper grids at temperatures of between -60 to -100 degrees C.

Sections were examined using a FEI Tecnai Transmission Electron Microscope at an accelerating voltage of 80 kV. Electron micrographs were recorded using a Gatan Orius 1000 digital camera and Gatan digital micrograph software.

Experimental Procedure for the STEM characterization

Sections on TEM grids were examined in FEI Helios UC SEM in Transmission Mode utilizing the STEM3++ detector with an accelerating voltage of 29 kV and a working distance of 5 mm. Images were processed in ImageJ 1.51j.



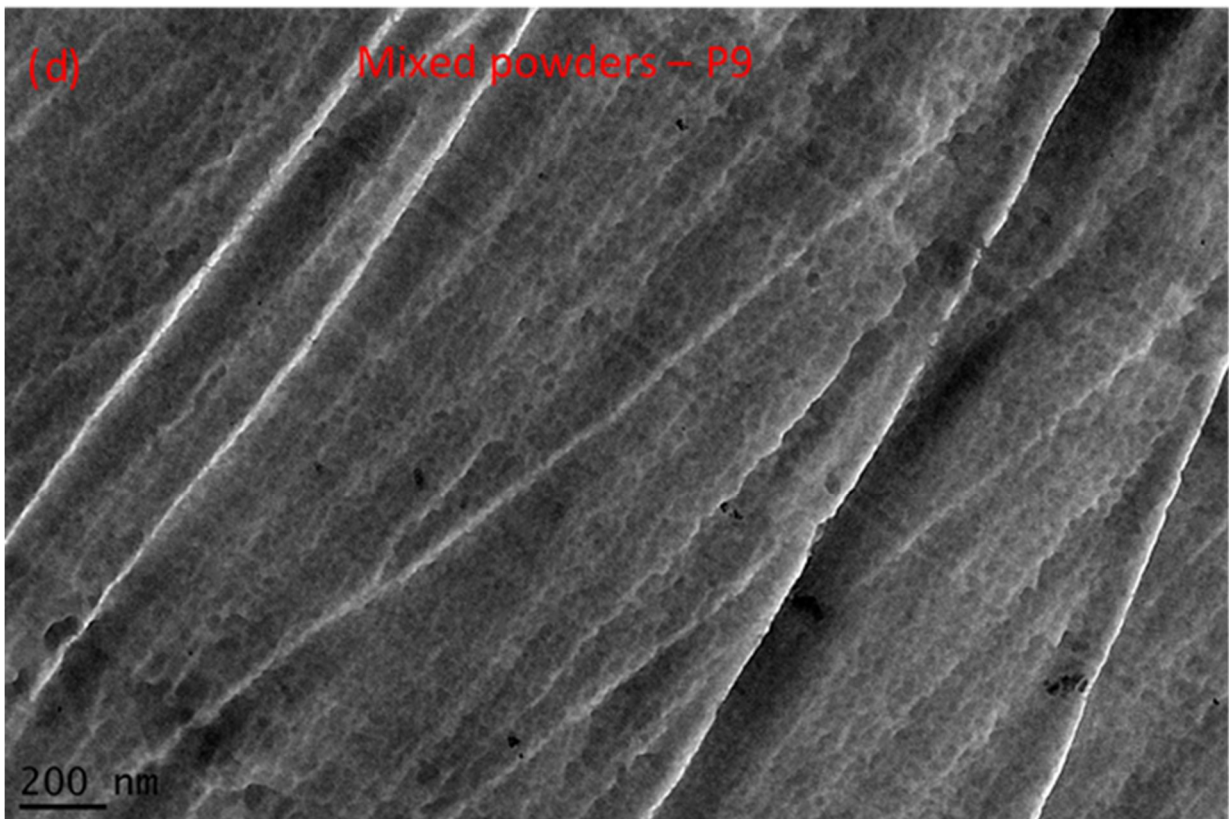
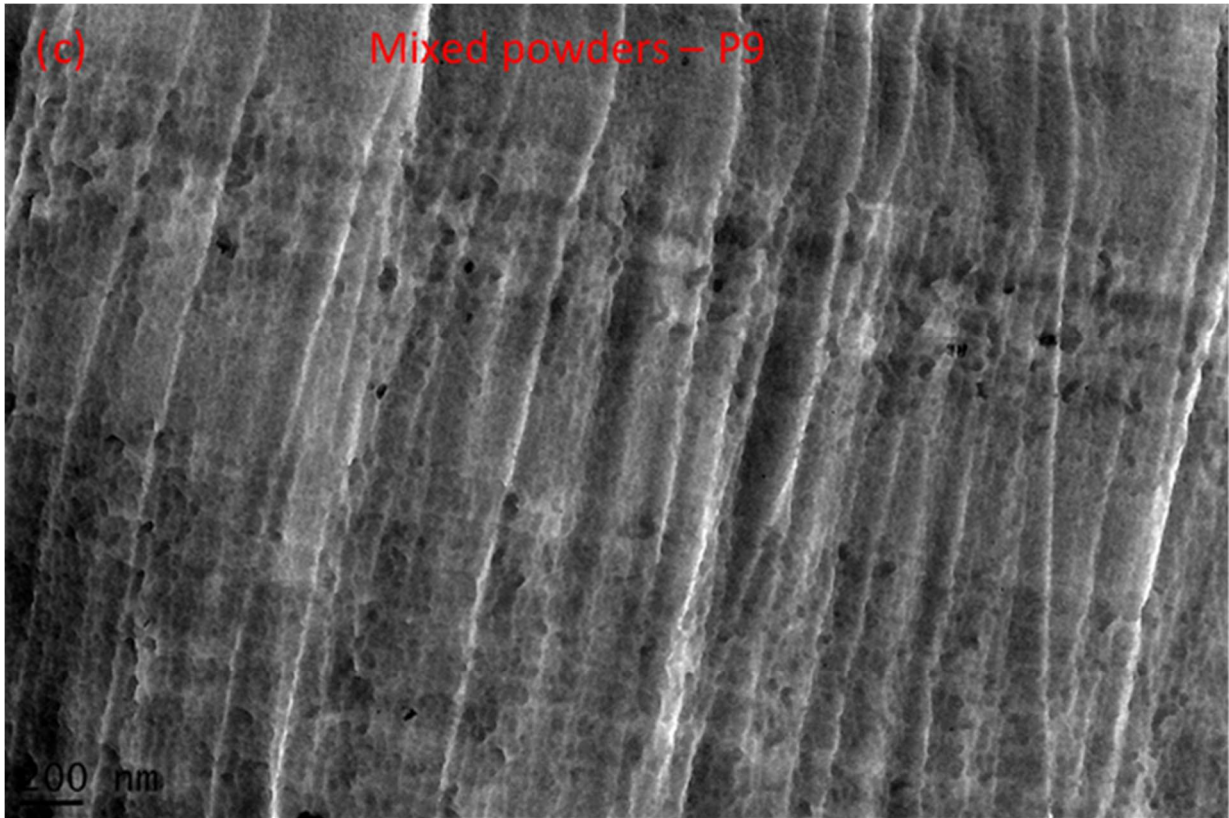
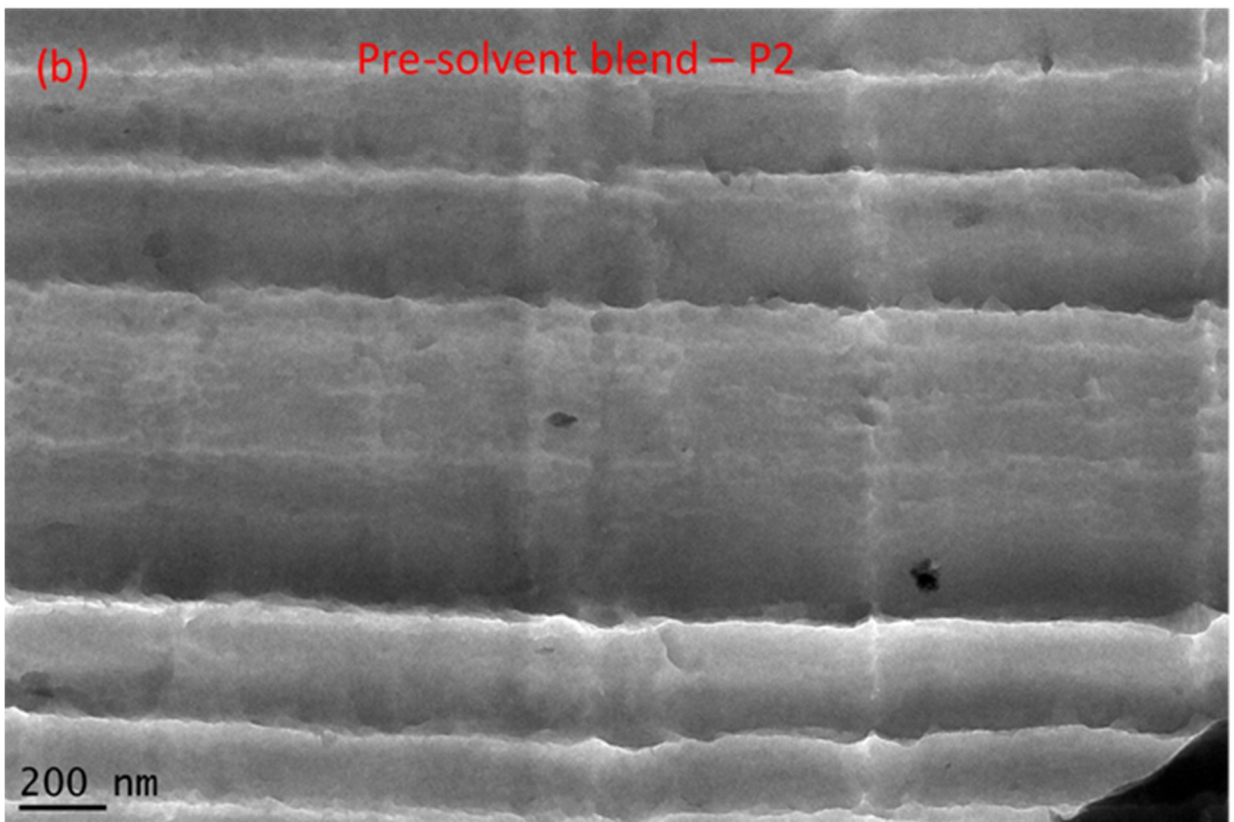
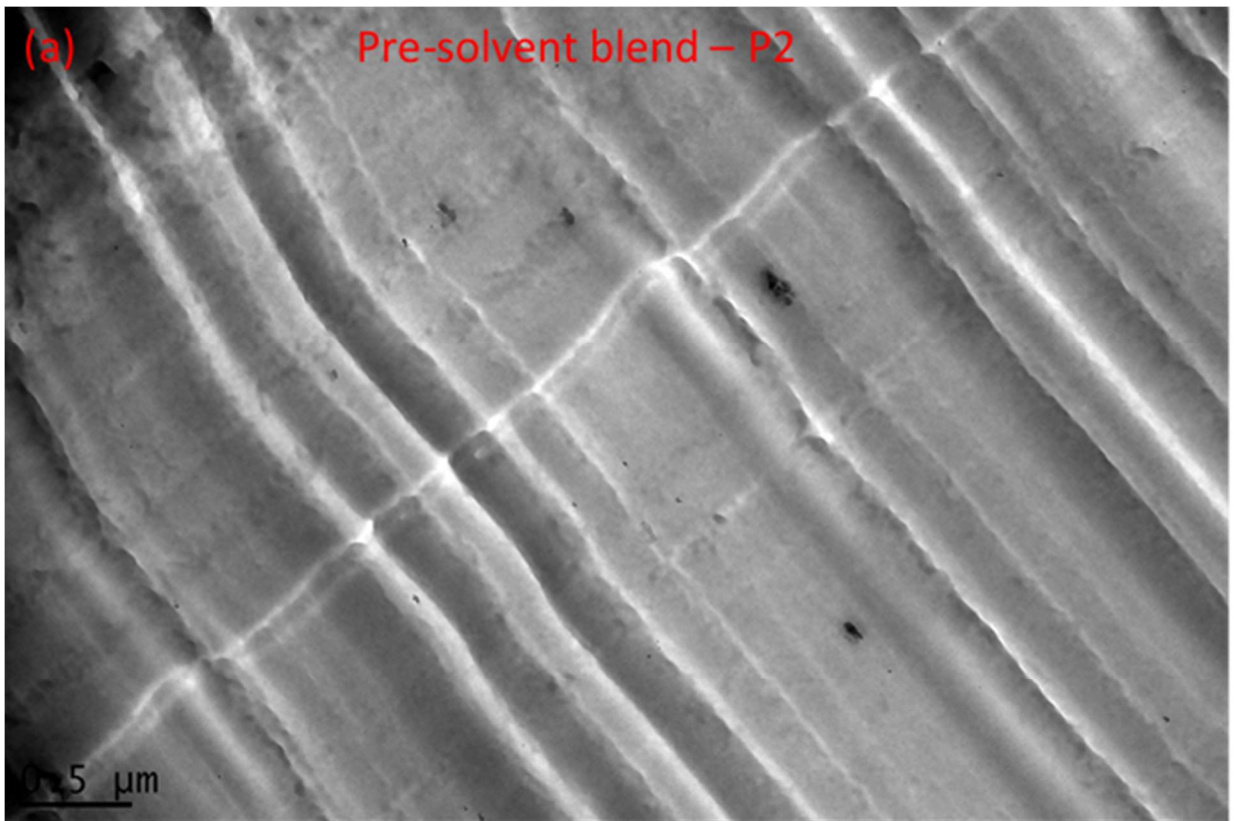


Figure S.I.7. TEM of composites processed from mixed powders: (a) and (b): P2; (c) and (d) P9



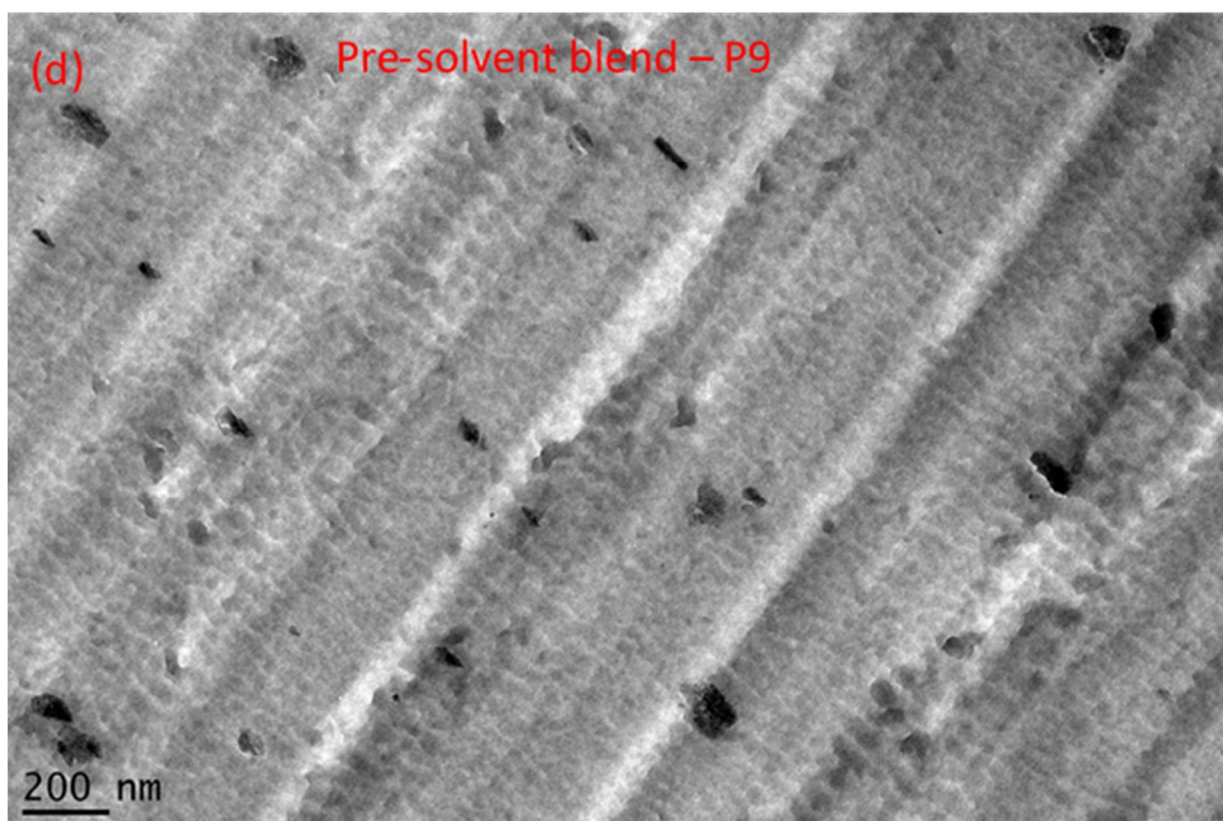
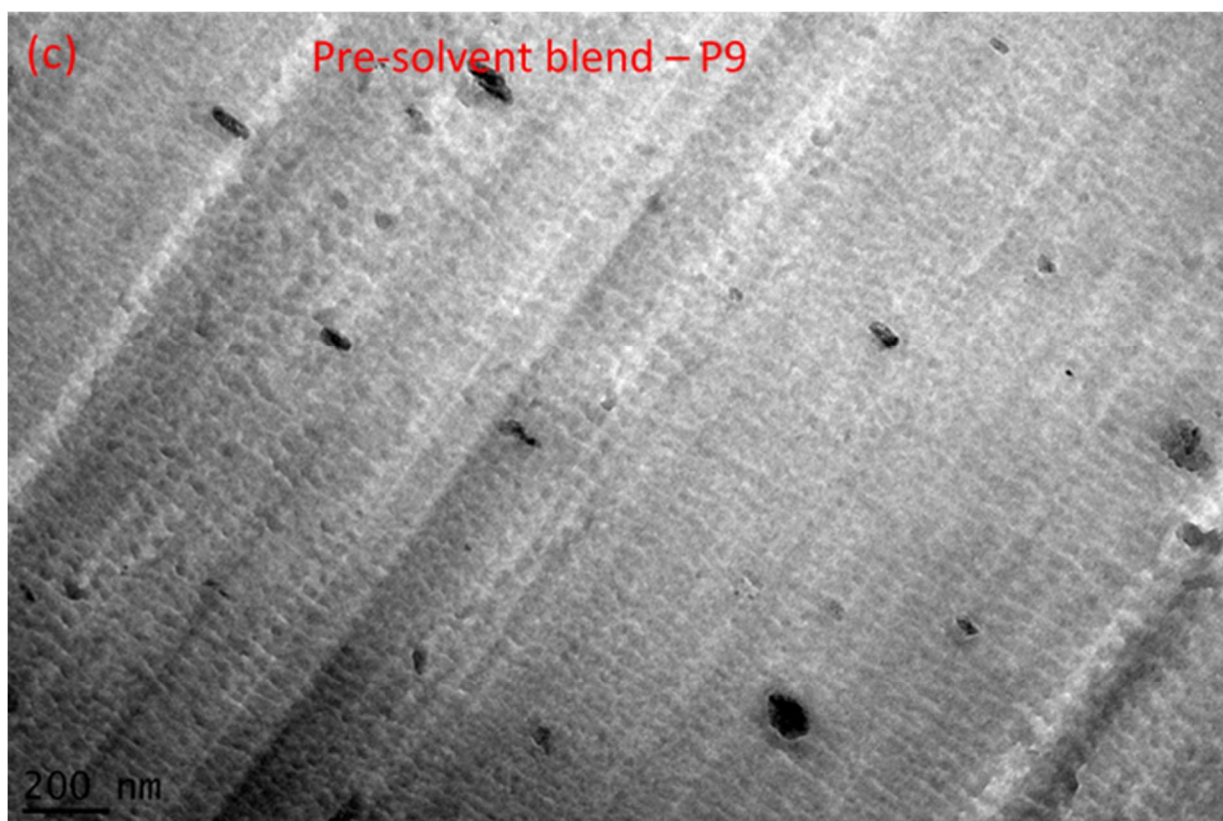


Figure S.I.8. TEM of composites processed from solvent-blend: (a) and (b): P2; (c) and (d) P9

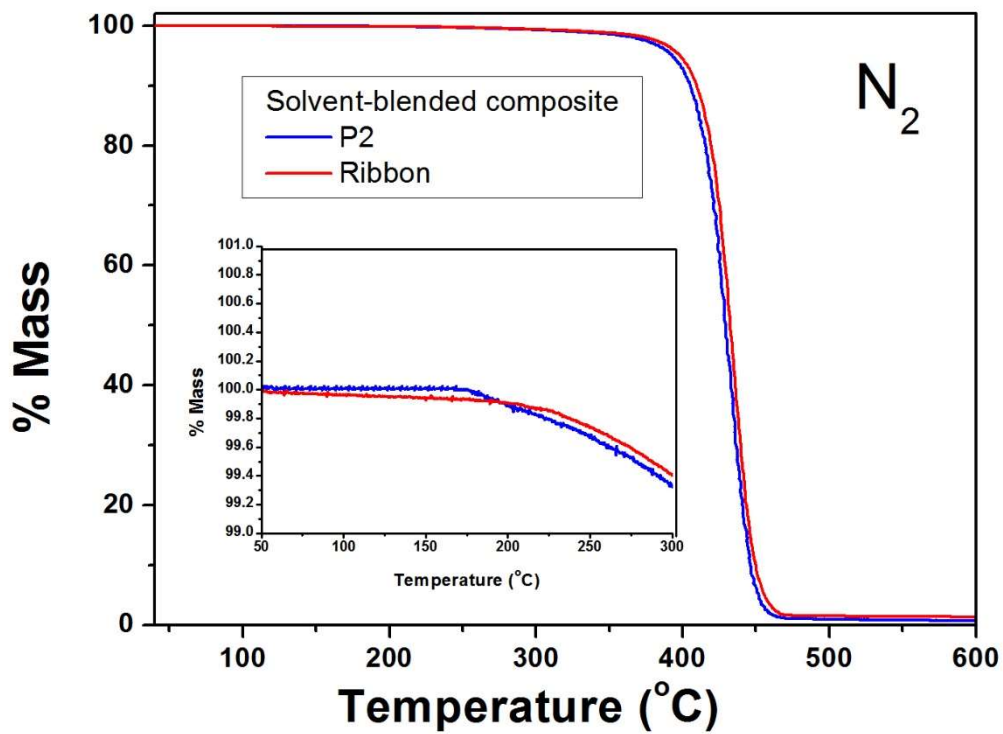


Figure S.I.9. Thermogravimetry measurements of pre-solvent-blended composites collected from P2 and ribbon.

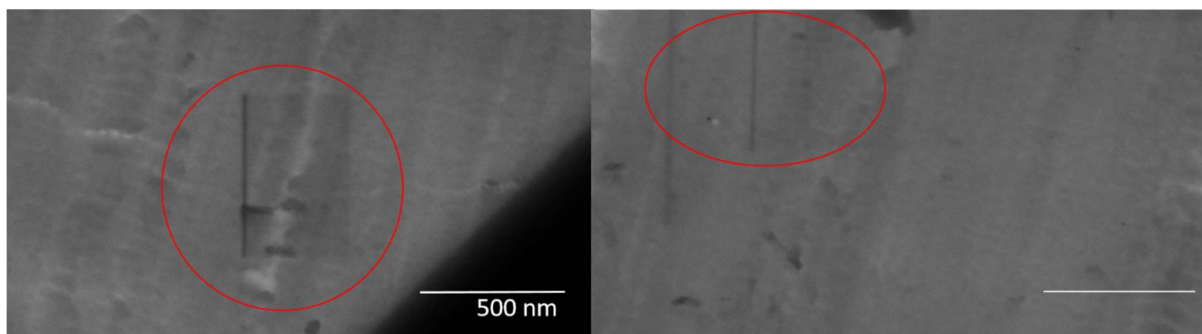


Figure S.I.10. STEM images showing contamination on surface of solvent processed samples caused by the electron beam highlighted by the red circles. The scale bars are both 500 nm.

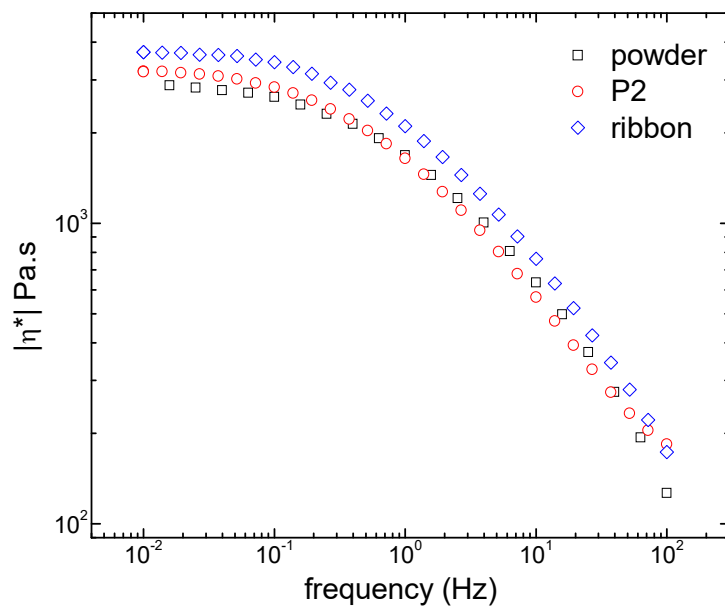


Figure S.I.11. Mechanical spectra measured at 200 °C of PS sample fed into the extrusion line (powder, squares), of PS sample collected at P2 along the extruder (P2, circles) and PS ribbon (ribbon, diamond).

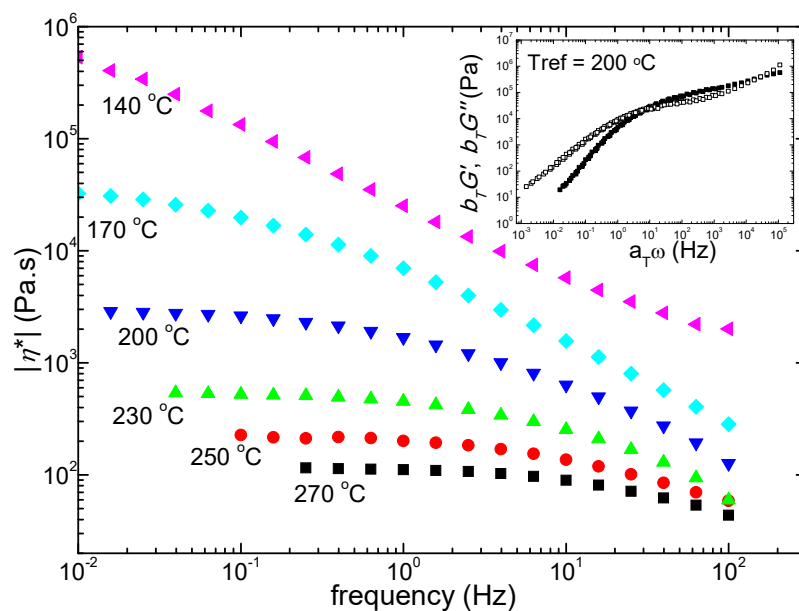


Figure S.I.12. Construction of the master curve of the PS matrix. Mechanical spectra measured at different temperatures indicated in the Figure are overlaid by shifting horizontally the curves with a factor a_T and vertically with a factor b_T to build the master curve plotted in the inset.

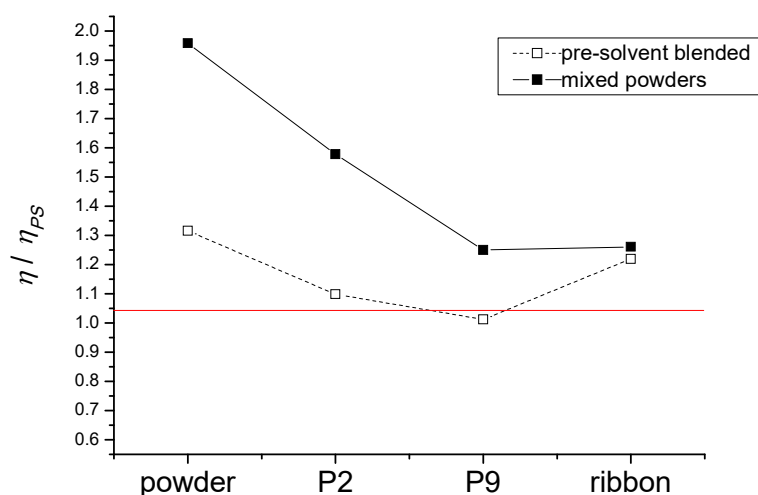


Figure S.I.13. Evolution along the extruder of the ratio between the zero shear viscosity of the composite η and the zero shear viscosity of the PS matrix η_{PS} for the two feeding formulations. The red line indicates the viscosity ratio predicted by the Einstein equation for a suspension of hard spheres in a Newtonian matrix.

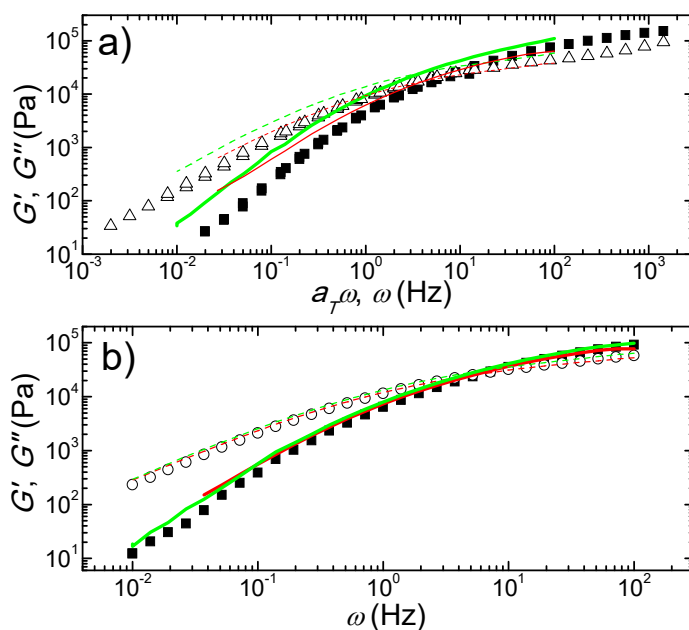


Figure S.I.14. Mechanical spectra of feeding powders (a) and of the corresponding extruded ribbons (b). Filled and empty symbols correspond to G' and G'' of the PS matrix respectively, whereas full lines and dashed lines correspond to G' and G'' respectively of the mixed powder samples (green) and the pre-solvent blended samples (red).